NASA

Technical Memorandum 80244

SMMR Simulator Radiative Transfer Calibration Model

I: Derivation

C. D. Calhoon, S. Link, M. Doyle and B. Krupp

AUGUST 1979

National Aeronautics and Space Administration

Goddard Space Flight Center
Greenbelt, Maryland 20771

TM 80244

SMMR SIMULATOR RADIATIVE TRANSFER CALIBRATION MODEL

I: DERIVATION

Charles D. Calhoon
Susan Link
Goddard Space Flight Center
Greenbelt, Maryland

Michael Doyle
Goddard Space Flight Center
and
University of Cincinnati
Cincinnati, Ohio

Brian Krupp
Systems & Applied Sciences Corp.
Riverdale, Maryland

August 1979

GODDARD SPACE FLIGHT CENTER
Greenbelt, Maryland

SMMR SIMULATOR RADIATIVE TRANSFER CALIBRATION MODEL

I: DERIVATION

C. D. Calhoon, S. I[illegible]k, M. Doyle, B. Krupp
Microwave Sensors Branch

ABSTRACT

Passive microwave measurements performed from earth orbit can be used to provide global data on a wide range of geophysical and meteorological phenomena. A Scanning Multichannel Microwave Radiometer (SMMR) is being flown on the Nimbus-G satellite. (A second SMMR was flown on the now inoperative Seasat-A satellite.) The SMMR Simulator duplicates the frequency bands utilized in the spacecraft instruments through an amalgamate of radiometer systems. Data taken using the SMMR simulator is being used by the scientific community for improving interpretation of the spacecraft data.

This document presents a calibration model developed for the SMMR Simulator Radiometer systems.

Portions of the material for this document were compiled and revised from the reports given in the Reference list.

CONTENTS

CONTENTS (Continued)

ILLUSTRATIONS

ILLUSTRATIONS (Continued)

ILLUSTRATIONS (Continued)

TABLES

SMMR SIMULATOR RADIATIVE TRANSFER CALIBRATION MODEL

I: DERIVATION

1.0 INTRODUCTION

1.1 General Background

The SMMR Simulator is an aircraft instrument which has been built to simulate the physics of the scanning multichannel microwave radiometer (SMMR) flown on the Nimbus-7 and Seasat satellites. This is an earth oriented microwave radiometer system which measures important oceanographic and meteorological characteristics needed to increase man's understanding of the ocean/atmosphere interface and its influence on world weather and climate.

The instrument provides data for the measurement of the ocean energy transfer parameters such as sea surface temperature, sea surface roughness (including foam, from which sea surface winds can be inferred), precipitation, and the sea/air heat exchange. Another objective is the mapping of polar ice coverages and the determination of the local age of the ice canopy.

The SMMR can also provide large scale data on land surfaces. Typical land surface data would include average soil moisture, extent of snowpack cover, and an indication of melting of snow on land areas having sufficient homogeneity (e.g., Great Plains of the United States).

The water present in the atmosphere, whether it is in the form of vapor, non-raining cloud water droplets, or rain, will affect the measured surface radiometric temperatures. These quantities must also be measured, therefore, in order that corrections to the surface data can be made.

The SMMR simulator duplicates the frequency bands utilized on the spacecraft instrument through an amalgamate of radiometer systems. These systems operate at center frequencies of 6.6, 10.7, 18.0, 21.0, and 37GHz. Each system operates in a receiver "time-share" mode such that readings are taken of both the vertically and horizontally polarized components of the received power. The antennas, mounted so as to provide a 45° view angle from nadir, all have 6° beamwidths making the system incident field-of-view approximately 1/10 of the aircraft altitude.

The SMMR simulator was flown on the NASA CV-990 during 1976, 1977 and 1978. Aircraft observations made with the SMMR simulator are useful in algorithm development, cross-calibration of the satellite data via underflight observations, high-resolution studies of the sea surface, and determinations of atmospheric water vapor and liquid water profiles.

The raw data obtained in a SMMR simulator observation are in the form of radiometer output voltages. These data must be calibrated before they can be analyzed in terms of the physical process producing the emission; that is, the radiometer output voltage must be related quantitatively to the intensity of the microwave radiation incident on the SMMR collection system.

This study is concerned with a theoretical analysis of the absolute calibration of the SMMR simulator and will serve as the basis for a system calibration procedure.

This study derives the "exact" calibration equation by applying microwave radiative transfer theory to the SMMR simulator collection system. For purposes of system calibration, it is assumed the power received by the radiometer system at the radome interface represents the absolute or true temperature of the scene being viewed. Any atmospheric phenomena or cross coupling aberrations are treated as part of the true temperature.

1.2 Instrument Heritage

Passive microwave measurements performed from earth orbit can be used to provide global data on a wide range of geophysical and meteorological phenomena. The use of such measurement techniques for remotely sensing earth's atmosphere and surface has been reviewed by Staelin and by Tomiyasu.[1,2]

The use of passive microwave imagers for remote sensing of earth surface parameters was started in earnest in 1967 with the installation of the electrically scanned microwave radiometer (ESMR) on-board the NASA CV-990 airborne laboratory.

The ESMR was used to study a variety of phenomena involving the surface of the earth and its atmosphere.[3-10] This imaging radiometer operates at a wavelength of 1.55 cm. It became

evident that the ESMR could be used to infer the extent, the concentration, and the age of sea ice; the extent, concentration and thickness of lake ice; rainfall rates over oceans; surface wind speeds over open water; particle size distribution in the deep snow cover of continental ice sheets; and soil moisture content in unvegetated fields.

The first experiments to use microwave techniques from earth orbit for remote sensing of geophysical phenomena were performed from the Soviet COSMOS-253 and COSMOS-384 satellite in 1968 and 1970, respectively.[11,12] The COSMOS experiments performed measurements at wavelengths of 8.5, 3.4, 1.35 and 0.8 cm for observing surface features such as ice in polar regions, and for observing atmospheric water vapor and liquid water over oceanic areas.

An ESMR has been operational, also at a wavelength of 1.55 cm, on the Nimbus-5 satellite since its launch in December 1972 and has been obtaining information on rainfall rates and sea ice cover on a global basis since that time.[13]

The other microwave experiment on Nimbus-5, the Nimbus-E Microwave Spectrometer (NEMS) performed nadir observations with five channels operating at wavelengths between 1.35 and 0.5 cm to obtain measurements, principally, of the atmospheric temperature profile, and of atmospheric water vapor and liquid water over oceanic areas.[14]

Several additional microwave experiments from earth orbit have been performed by the United States since Nimbus-5. The Skylab missions in 1973 and 1974 carried a radiometer operating at 21 cm wavelength.[15] Nimbus-6 launched in June 1975, carries an Electrically Scanned Microwave Radiometer (ESMR) operating at 0.8 cm wavelength, which is more sensitive to atmospheric water than the Nimbus-5 ESMR and scans the earth in a conical manner, keeping the angle of incidence of the observation constant to ease interpretation.[16] Nimbus-6 also carried a Scanning Microwave Spectrometer (SCAMS) which is similar to the Nimbus-5 NEMS, but has a scanning antenna for producing images.[17]

The radiation received by the ESMR imaging radiometers on-board a satellite is a combination of the contributions from both the atmosphere and the surface of the earth. In general it is not possible to separate these phenomena with the information in a single radiometer channel, thus requiring multi-spectral imaging techniques to unscramble the combined contributions of the atmosphere and the surface. An early effort in this direction has been accomplished on Nimbus 5 & 6 using NEMS and SCAMS.

A scanning multichannel microwave radiometer (SMMR) is being flown on the Nimbus-7 and Seasat satellites.[18] This is a ten-channel instrument in which the wavelengths to be observed are 0.8, 1.4, 1.7, 2.8, and 4.5 cm, and with both polarizations to be observed at each wavelength.

A summary of the properties of the surface of the earth and its atmosphere thought to be extractable from SMMR data are listed in Table 1-1.

The advent of the Space Transportation System (Space Shuttle) in 1980 will make feasible a new generation of microwave earth observations experiments. The increased volume and weight payload accommodations of the Shuttle will allow larger antenna structures to be used for earth observations experiments than previously possible. These larger antenna structures will provide substantially improved spatial resolution at wavelengths which have been used on prior experiments, and will make feasible the use of longer wavelengths not previously used for earth observations. Because of advancement in microwave radiometer technology at the shorter wavelengths, it will also be feasible to use shorter wavelengths for observation than previously possible.

1.3 Scientific Background

1.3.1 Physics of Microwave Radiative Transfer

At microwave frequencies (1-500GHz) and at temperatures typical of the earth and its atmosphere (200-300°K), the Rayleigh Jeans approximation for the intensity of thermal radiation from a blackbody is valid, thus the equation of radiative transfer for an isotropic, nonscattering medium can be written as

$$dT_B(\theta,\phi) = \gamma[T(X) - T_B(\theta,\phi)]$$

Table 1-1

Parameters to be Determined by SMMR

Parameter	Discipline/User Area	Remarks
Surface Winds (Ocean) Foam Cover Capillary Waves Large Scale Roughness	Oceanography, Meteorology Shipping	First System to Monitor Surface Winds Remotely.
Precipitation Rain Rate Rain/Snow Line	Meteorology, Shipping	Hurricane Classification Looks Promising
Water Vapor	Meteorology	Air Mass Discrimination Initial State Parameter for Forecast Models
Sea Ice Coverage Age Dynamics	Polar Studies, Meteorology, Military, Oceanography	Currently Operational Need for Continuity.
Soil Moisture	Meteorology, Hydrology, Military	Sampling Depth CA. 1/15 of a Wavelength.
Snow Cover (Over Land) Extent Ripeness	Meteorology, Hydrology	Strong Day/Night Differences Due to Varying Liquid Water Content
Cloud Physics Liquid Water Content Drop Size Parameters	Meteorology	Forecasting

where $T_B(\theta, \phi)$ is the radiance in the direction (θ, ϕ) expressed as equivalent blackbody temperature, T(X) is the thermodynamic temperature of the absorbing medium and is the absorption coefficient in units of X^{-1}. The derivative on the left side is along a ray path. The physical meaning of this equation can be understood by examining the effect on microwave radiation incident at an angle θ, on an absorbing slab of uniform temperature T_0, absorptivity γ_0, and of thickness δ as shown in Figure 1-1. The radiation from the other side consists of the incident radiation as attenuated by the slab $T_B e^{-\gamma_0 \sec\theta}$ plus re-radiation component $(1 - T_B e^{-\gamma_0 \delta \sec\theta}) T_0$. If the slab is opaque $(\gamma_0 \delta \sec\theta = \infty)$, the radiation emerging is characterized by the thermodynamic temperature of the slab independent of the intensity of the incident radiation.

There are three major contributions to γ in the atmosphere: water vapor, liquid water, and molecular oxygen. Figures 1-2, 1-3, and 1-4 show the approximate magnitude of each of these contributions. Detailed discussions of each of these can be found in Gunn and East (1954),[21] Meeks and Lilley (1963),[22] and Staelin (1966).[23] Figure 1-5 shows the typical microwave earth viewing geometry. The observed brightness temperature is

$$T_B = \int_0^H T(h) \frac{dt(h)}{dh} dh + t(H) [\epsilon T_0 + (1 - \epsilon) T_S],$$

$$\text{where } t(h) = e^{-\int_0 \gamma(x) \sec\theta \, dx},$$

T(h) is the atmospheric temperature profile, H is the altitude of the observation, ϵ is the emissivity of the surface, T_0 is the thermodynamic temperature of the surface, and T_S is the reflected sky brightness. At frequencies of about 50GHz the variations in ϵ dominate the variations in T_B over the earth's surface. The major contribution to variations in ϵ is liquid water with its extremely large dielectric constant at microwave frequencies. Figure 1-6 shows the real part k′ and the k″ of the dielectric constant of both fresh and sea water at 20°C as calculated from the data of Lane and Saxton (1952).[24] Conductivity data from the International Critical Tables (1928)[25] are included as k in Figure 1-6.

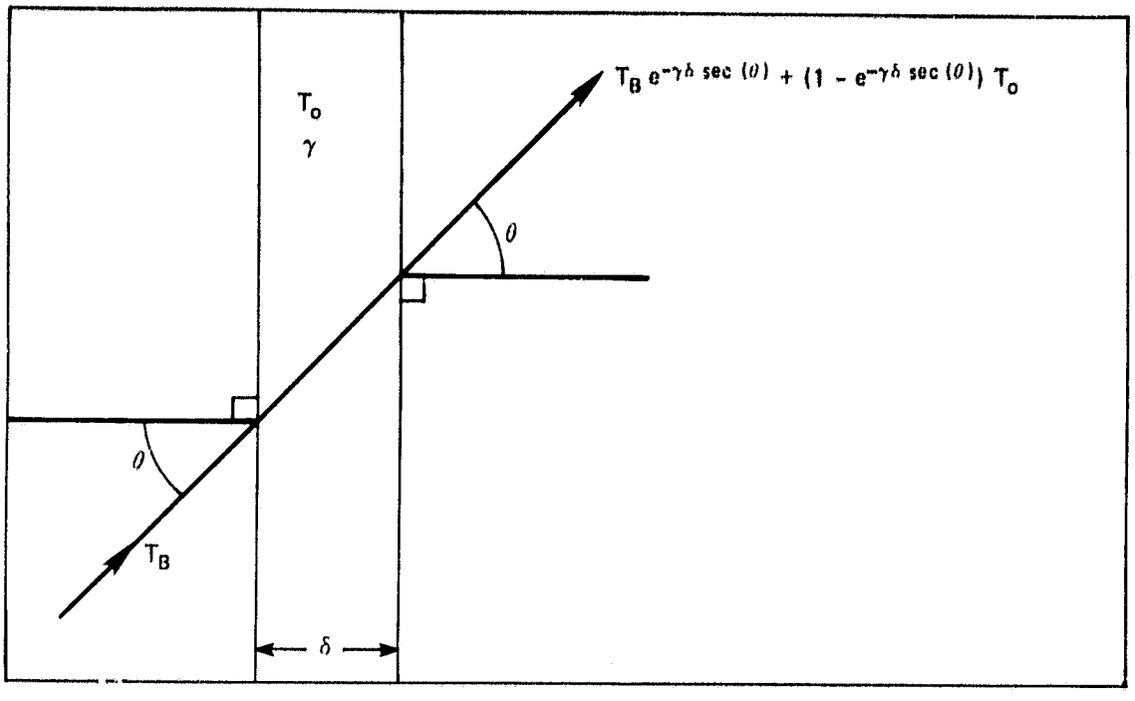

Figure 1-1. The Effect on Microwave Radiation at an Angle, θ, on an Absorbing Slab of Uniform Temperature Absorptivity and Thickness

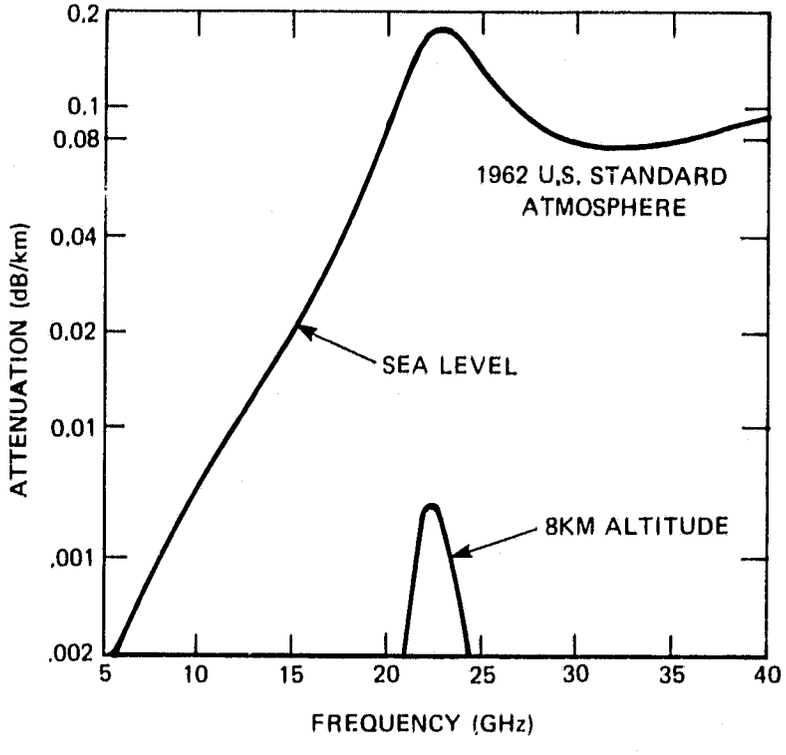

Figure 1-2. Microwave Attenuation Due to Atmospheric Water Vapor

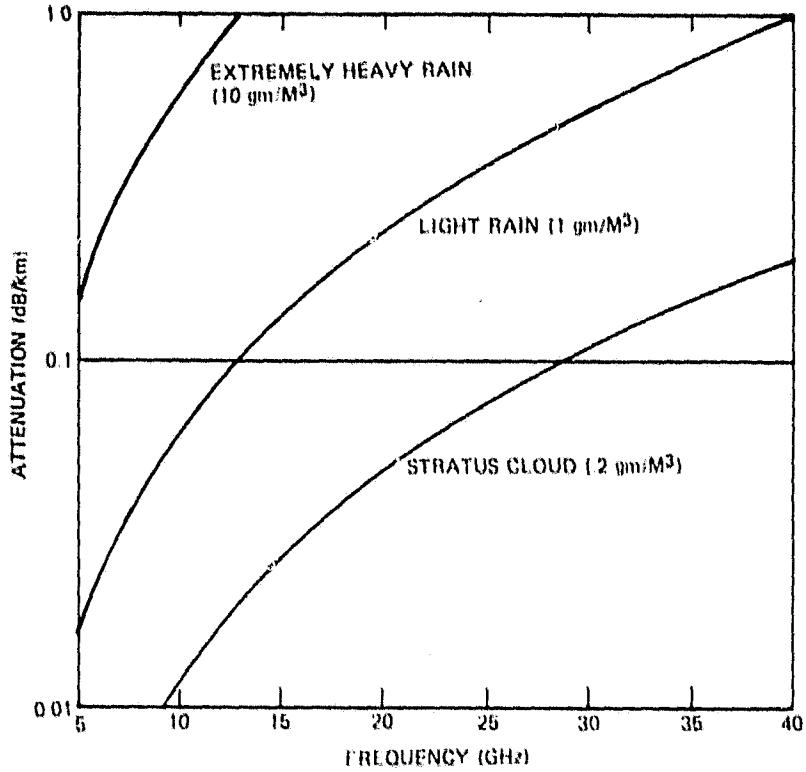

Figure 1-3. Microwave Attenuation Due to Liquid Water (Approximate)

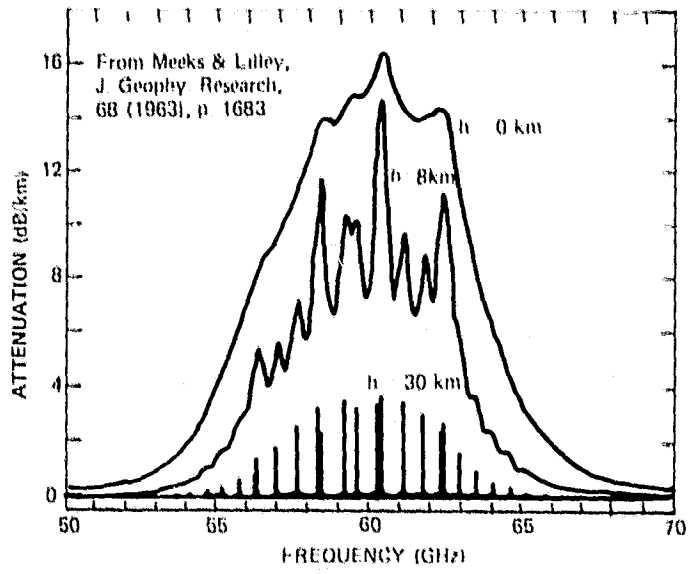

Figure 1-4. Microwave Absorption by Atmospheric Oxygen

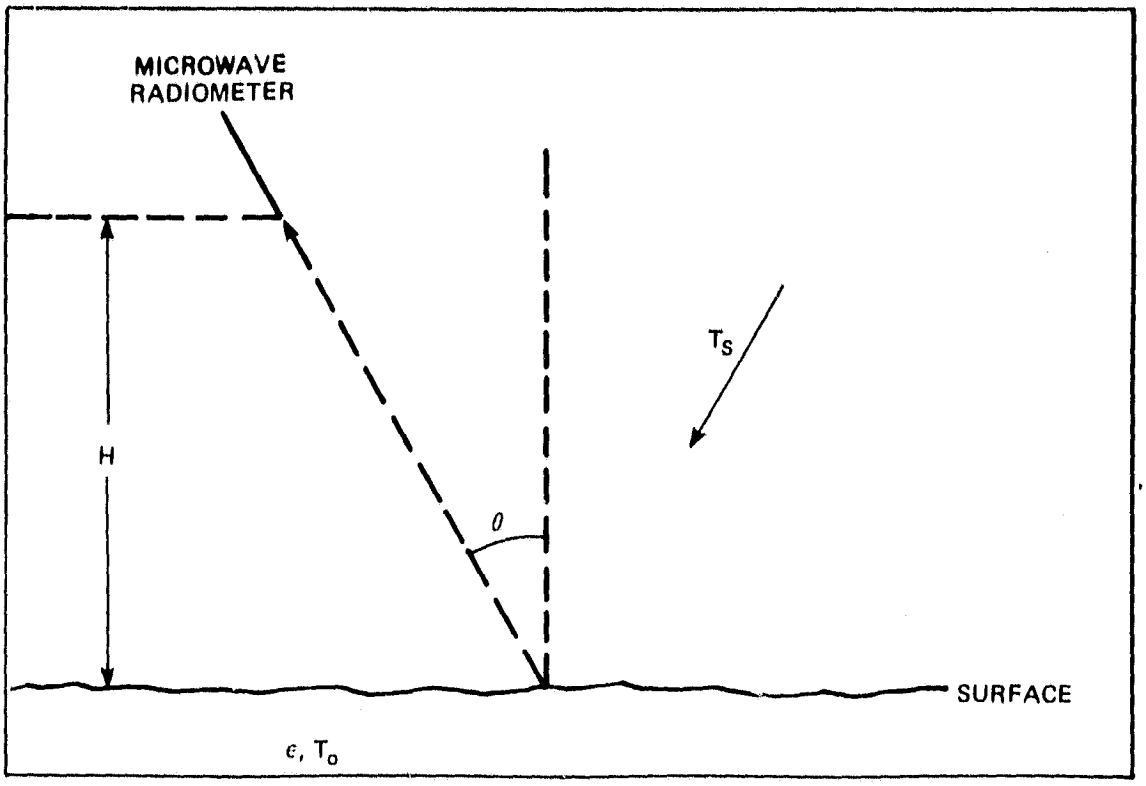

Figure 1-5. Typical Microwave Earth-Viewing Geometry

The emissivity can be calculated for smooth water for any angle and polarization from electromagnetic theory (Jackson 1962).[26] Figure 1-7 shows the emissivity as a function of frequency at 20°C for sea and fresh water for viewing at nadir, and at 45° for vertical and horizontal polarization. The dependence of the primary ϵT_0 term on the surface temperature is given in Figure 1-8 for nadir viewing (incidence angle = 0°) and for a 55° incidence angle for vertical polarization. The sensitivity to surface temperature is small, particularly near 1-1.5 cm wavelength. The maximum sensitivity to surface temperature occurs near a wavelength of 5 cm.

The emissivity of the surface also depends on surface wind because of the generation of roughness and foam. The roughness effect has been investigated by Hollinger (1971)[22] and others. There is little roughness effect for viewing near nadir and near 55° with vertical polarization. The effect is maximized by viewing the surface obliquely with horizontal polarizations. At a 55° incidence angle the effect is about 1°K increase in brightness temperature for each meter per second

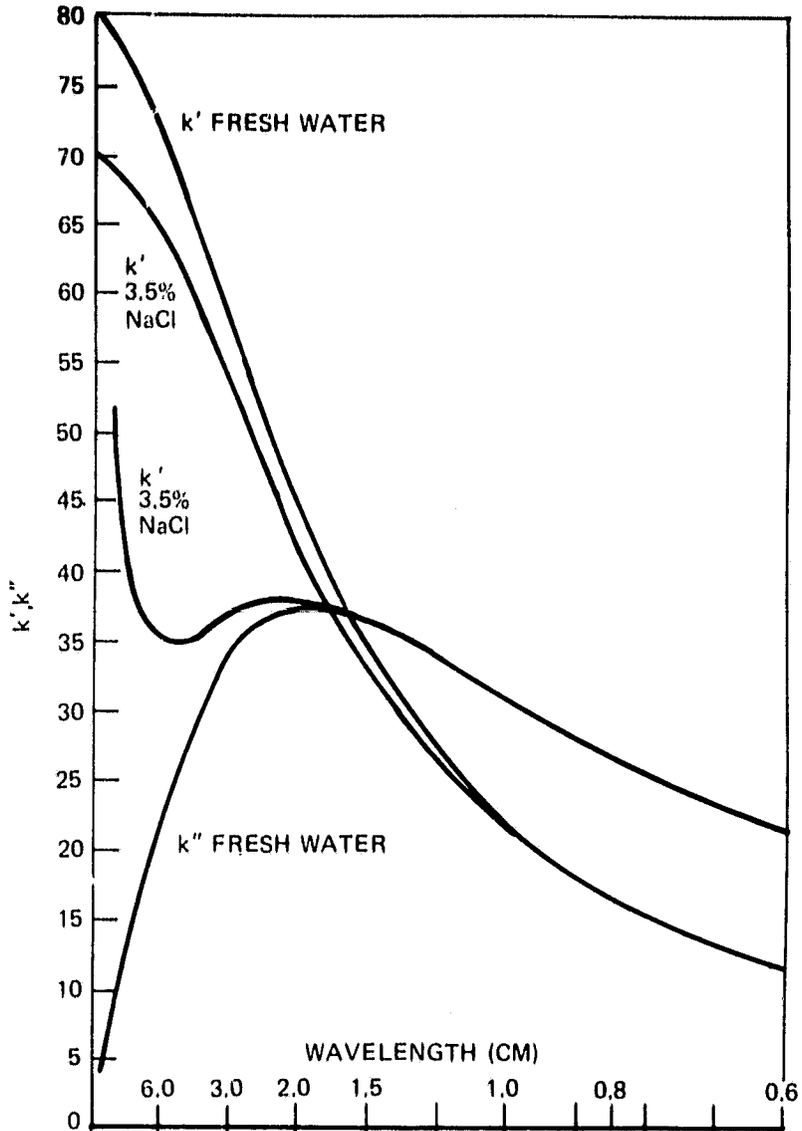

Figure 1–6. Dielectric Constant of Water
$k = (k' + ik'')$ at 20°C

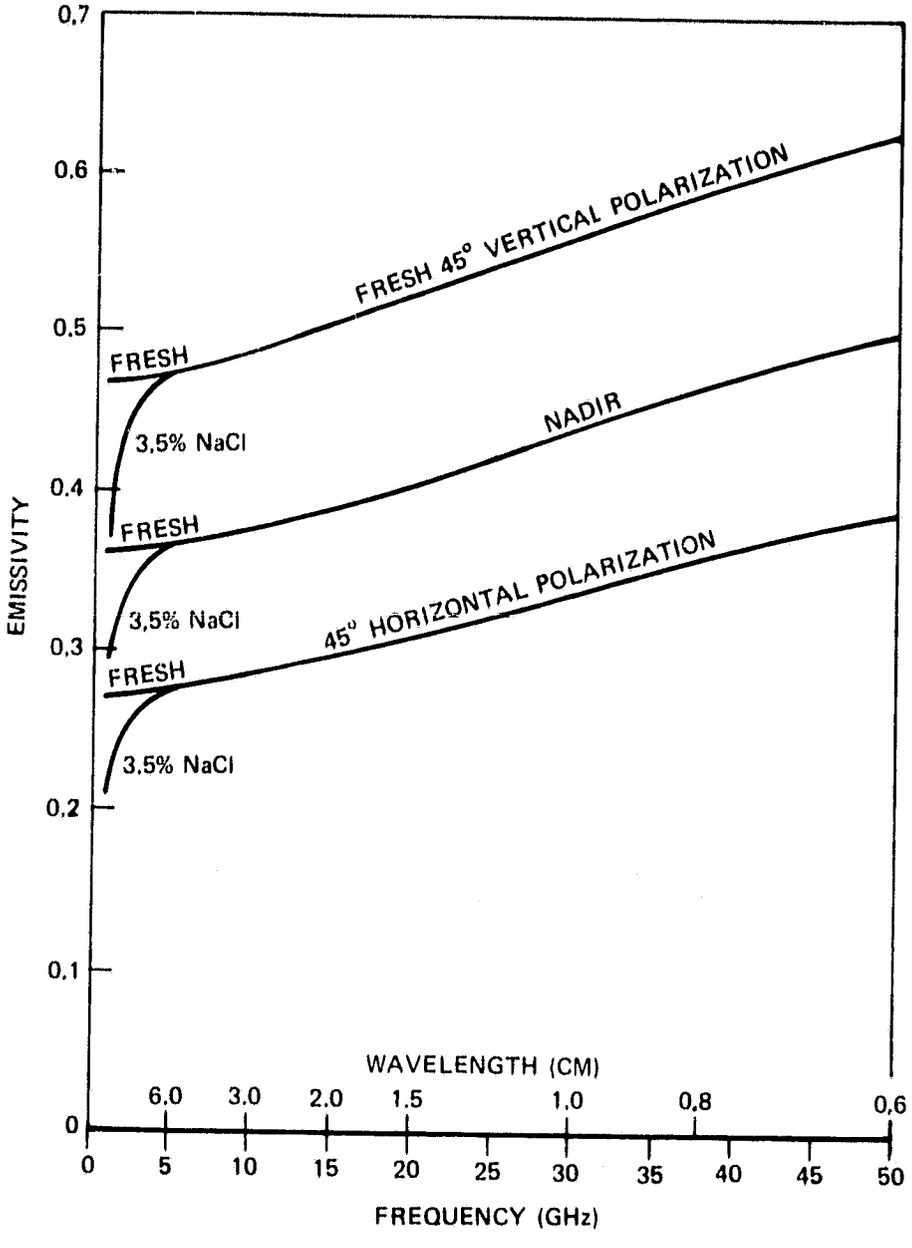

Figure 1-7. Emissivity of Water at 20°C

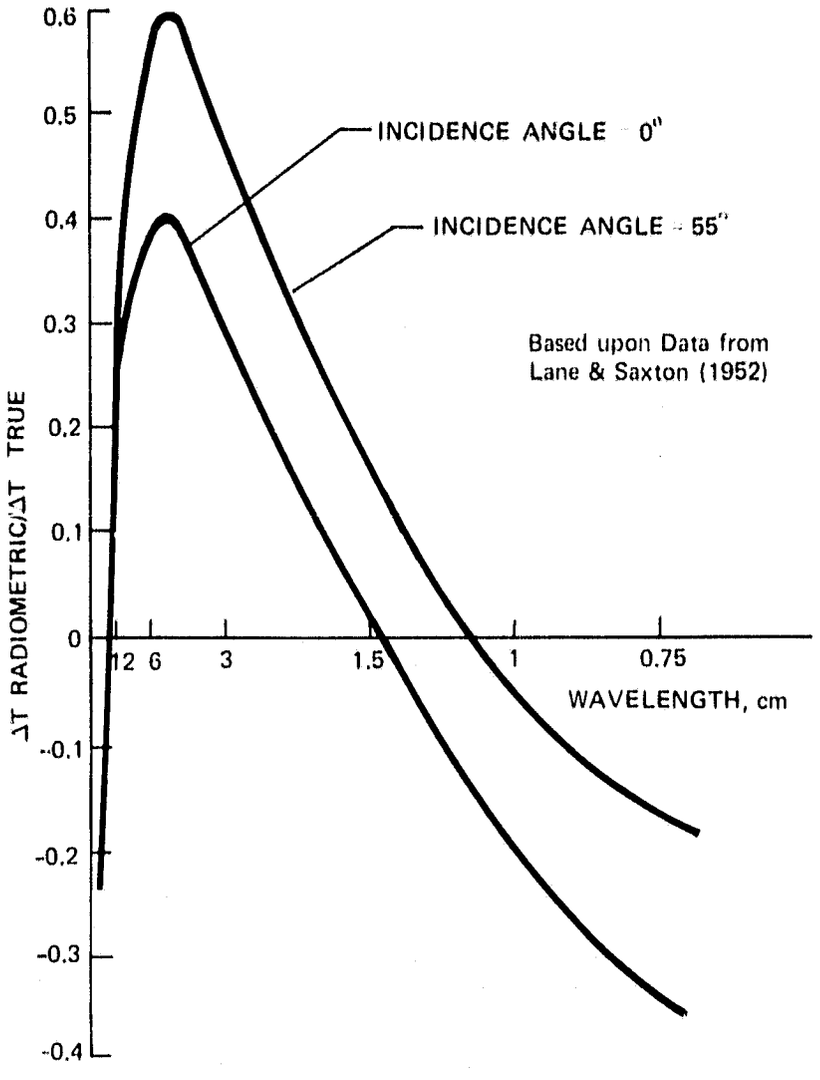

Figure 1-8. Radiometric Temperature Sensitivity for Calm Seawater, Vertically Polarized Component

increase in wind speed. Foam, which has been investigated by Nordberg, et al., (1971)[28] and Von Melle, et al., (1973) has an emissivity near 0.8. The foam coverage increases roughly 2% for each meter per second increase in wind speed about 7 m/s. Neither effect shows strong frequency dependence through the microwave range. The effect of surface wind is summarized in Figure 1-9.

The emissivity of a land surface is typically greater than 0.9 so the brightness temperature contrast between land and water is greater than 100°K; therefore, the outlines of the continents will be quite visible in the SMMR data. This will provide a convenient geographic reference but little scientific value. However, in areas with little vegetation, the moisture content of the soil affects the microwave signature markedly. Figure 1-10 (from Reference 29) shows data taken with the aircraft model of the ESMR on two flights over test feilds near Phoenix, Arizona. Note that for this soil (a clay loam) the brightness temperature decreases rapidly for soil moisture values greater than about 20% by weight. There is a large scatter in the data but soil moisture estimates to the nearest 5% are possible in the 20-40% range. Such measurements may provide useful information in the arid regions where large areas with little vegetation are found.

In contrast with soils, the liquid water content of snow seems to increase the radiometric brightness (Reference 30). Very dry snow, less than 1% free water content by volume, showed anomalously low emissivities, less than 0.5 at 26GHz, whereas moist snow, greater than about 5% free water content by volume, showed emissivities greater than 0.9. This effect has been qualitatively observed at 19.35GHz (Reference 31). The effect is not understood theoretically nor adequately characterized experimentally, as yet. Nonetheless, it offers an interesting possibility of observing the onset of melting of the snow in the spring, and of mapping the snow cover in winter.

Like land/water boundaries, ice shows a significant emissivity contrast with water but unlike the case of land/water boundaries are quite variable and their locations are definitely of interest

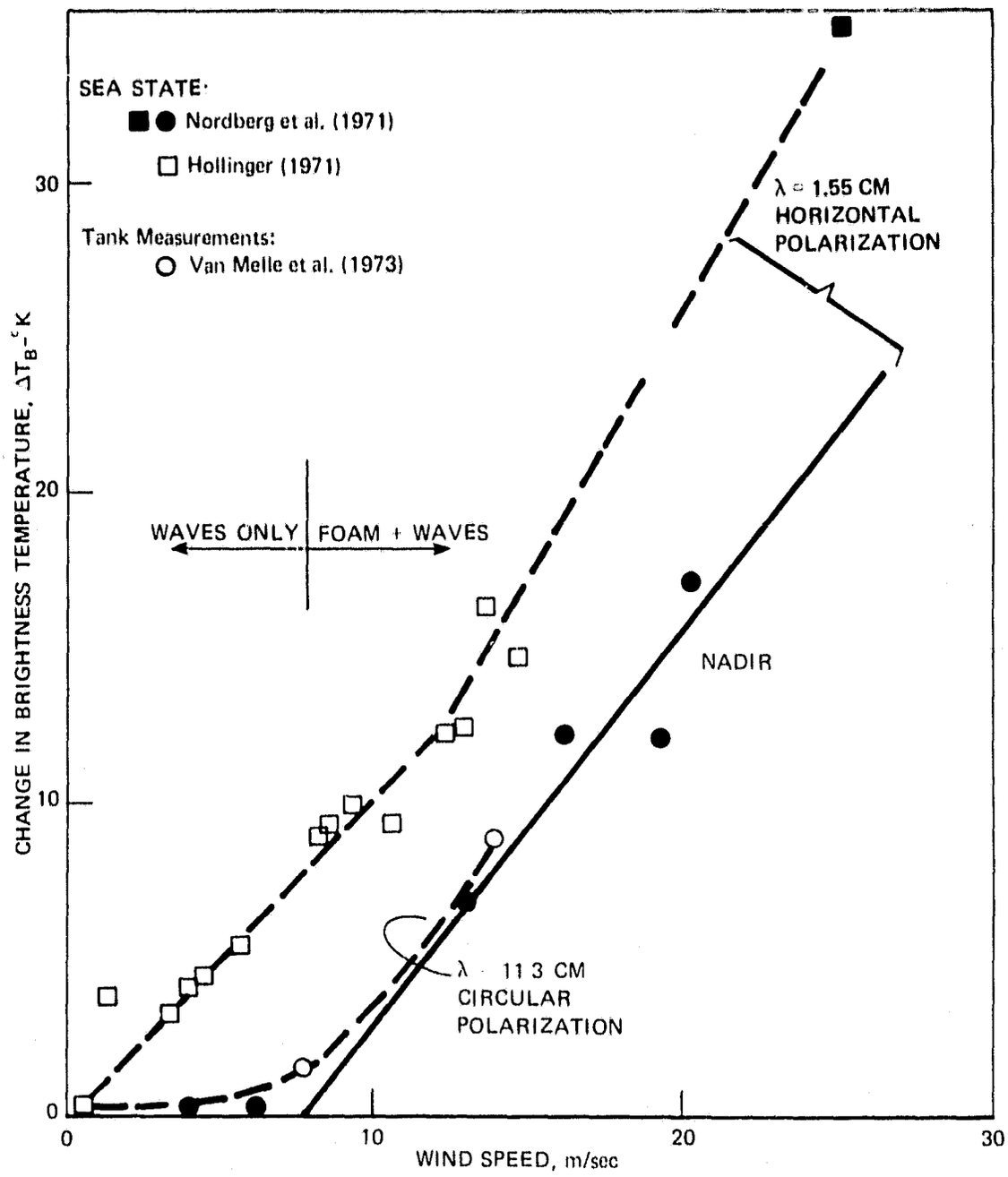

Figure 1-9. Dependence of Brightness Temperature on Sea State

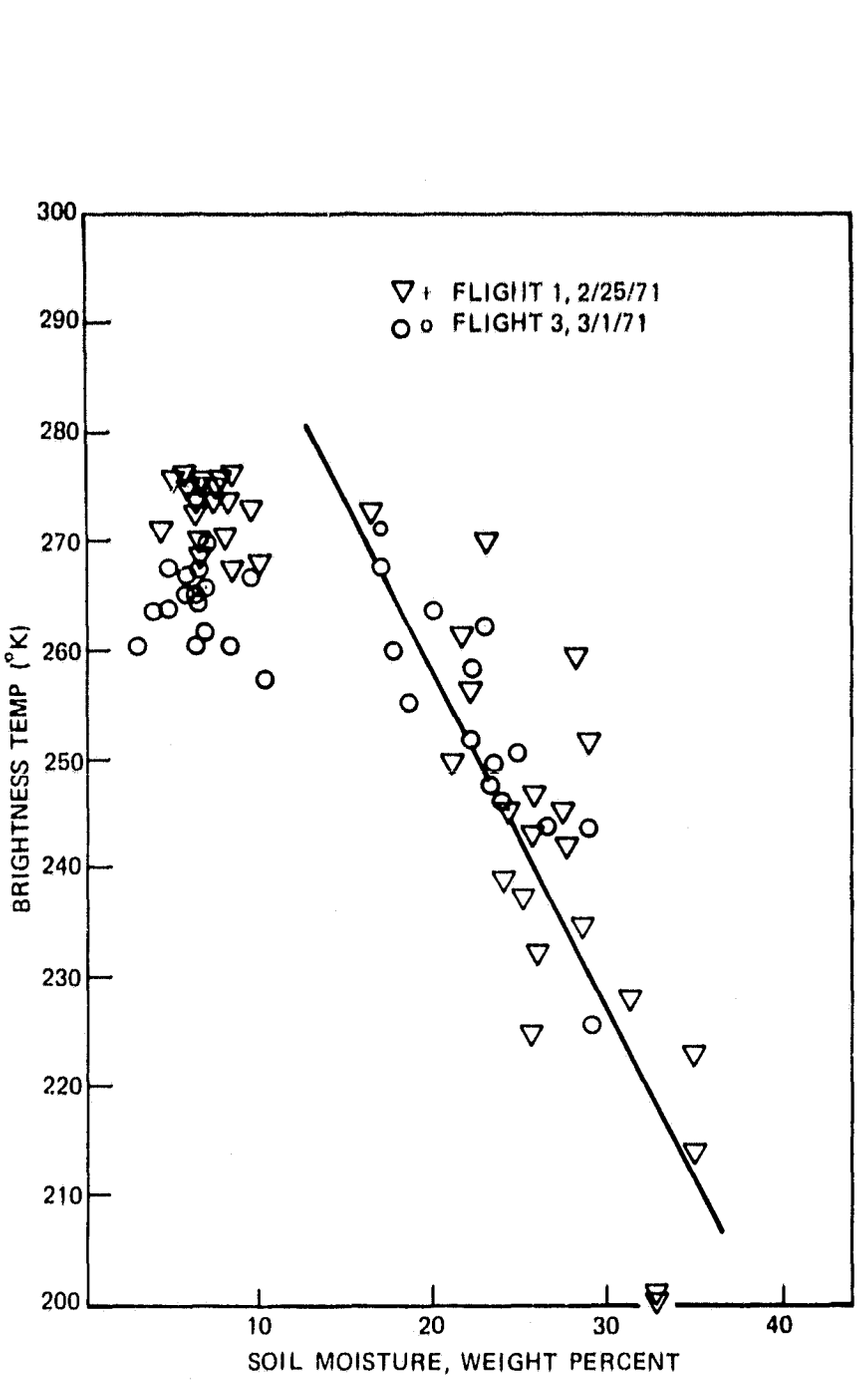

Figure 1-10. Brightness Temperature Results of Bare Fields with Clay Loam Soils, 1.55 cm Radiometer, Phoenix, Arizona

to the meteorological and maritime communities. These features are frequently covered with cloud which makes visible or infrared remote sensing difficult; it is expected that these clouds will rarely, if ever, be dense enough to alter significantly the microwave images. The ice/water boundary has been observed through clouds (Reference 31). The sea itself has been observed to have emissivity variations (Reference 31). These variations, at this point, are thought to be related to age, first year ice being more emissive than multi-year ice. Figure 1-11 shows the spectral nature of these two types of ice. Note that the contrast between the two types seems to increase linearly with frequency. In the non-beam filling situation, this effect will contribute about 10% uncertainty to estimates of the percentage of ice within one resolution element.

1.3.2 SMMR Parameters to be Measured -- Frequency Selection

The parameters of interest for the SMMR are given below.

Freq. GHz	Wave Length Cm	Vertical Channel	Horizontal Channel
6.6	4.54	Sea temperature	Separation of surface atmosphere effects; surface winds
10.69	2.81	Rain water in heavy rain; separation of surface and atmospheric effects	Rain water in heavy rain; surface winds
18.0	1.67	Rain water in light rain; separation of surface and atmospheric effects	Rain water in light rain; surface winds
21.0	1.43	Tropospheric water vapor; separation of surface and atmospheric effects	Tropospheric water vapor; surface wind
37.00	0.81	Surface winds (through foam); sea ice/polynyas; old ice/new ice	Same as for vertical channel

The secondary objective is to measure soil moisture (6.6 to 21.0 GHz).

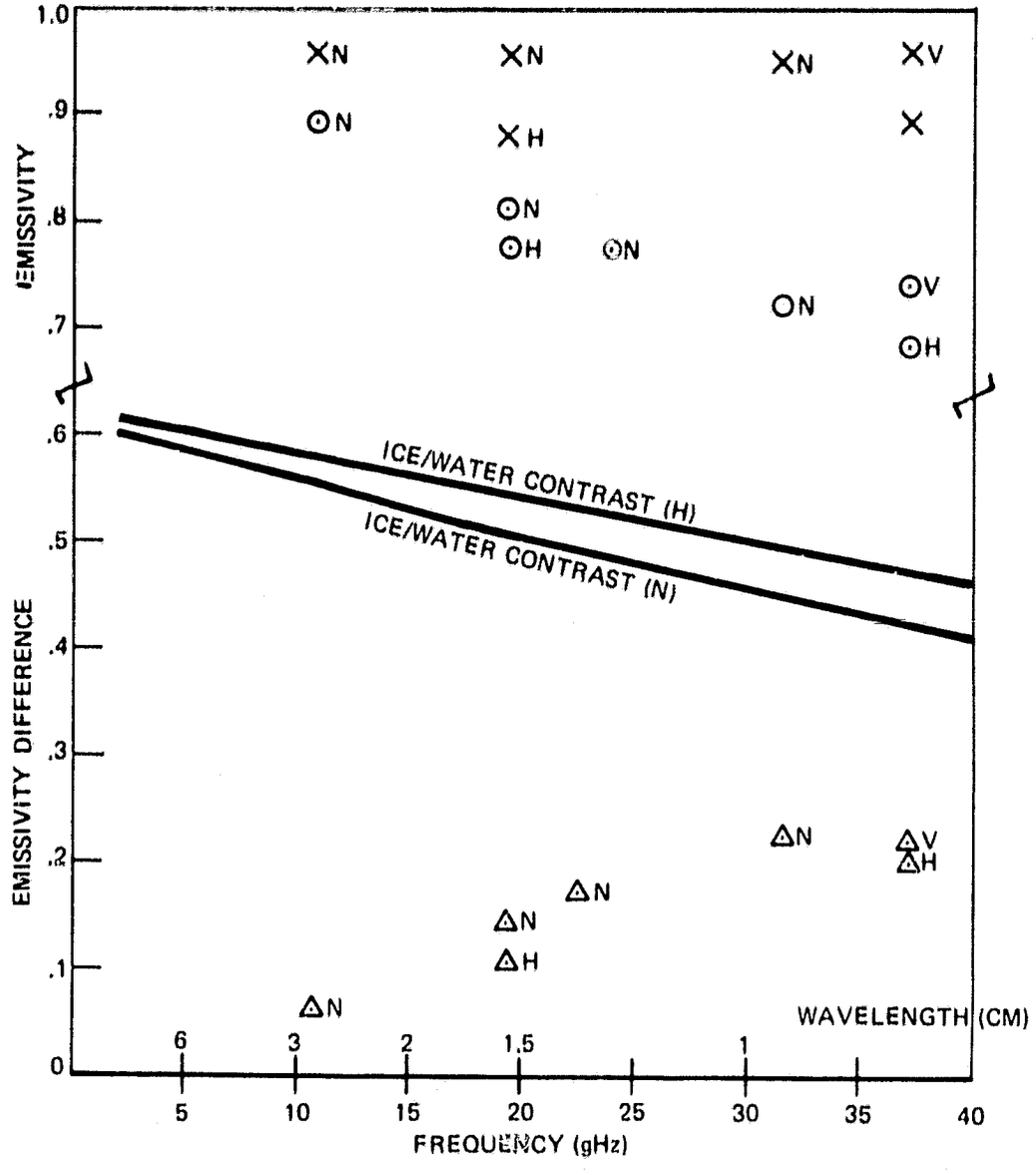

Figure 1-11. Microwave Emissivity Contrasts of Old and New Ice

The primary source for the sea-surface temperature data will be the vertically polarized 6.6 GHz channel. The basic reason for choosing this frequency is its proximity to the peak of the sensitivity curve and a spacecraft design limitation. Two of the major sources of interference, surface foam and heavy rain clouds, are polarization independent, so the horizontally polarized 6.6 GHz channel will be used to provide corrections for these two particular effects. Sea-surface roughness, however, appears to have some dependence on polarization. Since sea-surface roughness is frequency dependent, higher frequency channels that are not affected by the thermodynamic temperature of the water will be used to provide roughness data. The highest frequency channels (37.00GHz) will not be used for this purpose since they are too far removed from the 6.6GHz channels to permit extraction of roughness data by means of the frequency dependence. Although the correction for varying water-vapor concentration at 6.6GHz is not expected to be large in comparison with the corrections previously mentioned, it is nevertheless important. Data from the 21.0GHz channels will be utilized for making this correction. Heavy rainfall will also interfere with the determination of the sea-surface temperature because it will contribute to the sea-surface roughness. It may be possible to use data from the rainwater channels to correct for this interference; the range over which this will be possible remains to be determined

The 37GHz channels will obtain data on the percentage of foam cover, which will be the prime source for determinations of sea-surface windspeeds (> 7 m/s). This type of determination can be performed best with data from the 37GHz channels, rather than from channels at 19.35GHz where observations have already been made with a mapping radiometer, since the higher frequency is better suited for observing thin layers of foam. Heavy rainfall will render the 37GHz channels useless for wind-speed measurements; under such conditions it may be possible to observe the foam cover at longer wavelengths if the rain striking the sea surface does not obscure it. The 37GHz channels also play an important role in the determination of open water in the polar ice canopies and in the determination of the age of the polar ice.

In addition to the interference caused by raindrops striking the sea surface, the effect of water vapor in the intervening atmosphere must also be properly considered. This is handled best by a real-time measurement approach, with the 21.0GHz channels, which is adjacent to the water-vapor line, used for accurate water-vapor corrections under a wide variety of humidity conditions.

A three-frequency approach has been chosen for the determination of the liquid water in the atmosphere, since this will permit detection of water droplets over a wide range of droplet sizes in both raining and nonraining clouds. Another important advantage of this approach is that it permits the wavelength dependence of the water-droplet signature to be utilized for the unfolding of this particular feature from the rest of the interwoven data. The frequencies chosen for this purpose must be sufficiently removed from the water-vapor line so that the interference is reduced to a manageable level. A frequency of 10.69GHz (a radio-astronomy frequency) has been chosen because it possesses maximum sensitivity to the water droplets found in heavy rainfalls; 18GHz has been selected for lighter rain and also its small response to water-vapor variations; and 37GHz has been selected for determining the amount of liquid water in non-raining clouds because the droplets in this type of cloud are smaller than in raining clouds and because there is an atmospheric window at this frequency.

Dual polarization at all frequencies has been utilized because it will facilitate the separation of surface and atmospheric effects since, in general, the former exhibit polarization and the latter do not.

It also should be emphasized that the dual-polarization approach dictates that observations must be made at angles away from the nadir; the optimum zenith angle for these observations, aside from other considerations, appears to be approximately 50°.

2.0 SMMR SIMULATOR RADIOMETER SYSTEMS DESCRIPTION

2.1 Basic Radiometer Operation

The radiometer systems comprising the SMMR simulator are all of the Dicke type. Each of the radiometers operates in a "receive time share" mode so that data are taken from both the

vertically and horizontally polarized components of the received signal power (T_A). Each radiometer system consists of the following subsystems (Figure 2-1):

a. Antenna and Radome

b. Switching and Calibration Network

c. Receiver Electronics

d. Post Detection Processor

e. Power System

f. Timing and Control System

A detailed description of these subsystems is given in Reference 36.

2.2 Subsystem Description

2.2.1 Antenna Radome

The antenna system gathers the incident power and channels this power into horizontally and vertically polarized components. All antennas have a beamwidth of 6° ± 1° at the 3dB points. All planes exhibit low sidelobe levels, nominally -30dB maximum. Beam efficiency (pe centage of received energy between first nulls) is at least 90%. For those antennas which are ir stalled in the microwave antenna housing ("sled") carried beneath the aircraft body a radome i used for aerodynamic closure.

2.2.2 Switching and Calibration Network

The switching and calibration network (SCN) performs the following functions:

1. supplies radiometer RF modulation ("Dicke" operation)

2. provides for received electronics time-sharing by switching between antenna polarizations, and

3. supplies reference temperature signals near the extremes of the system dynamic range.

The SCN consists of the following subsystems.

a. switching block

b. liquid nitrogen load

Its configuration is shown in Figure 2-2A.

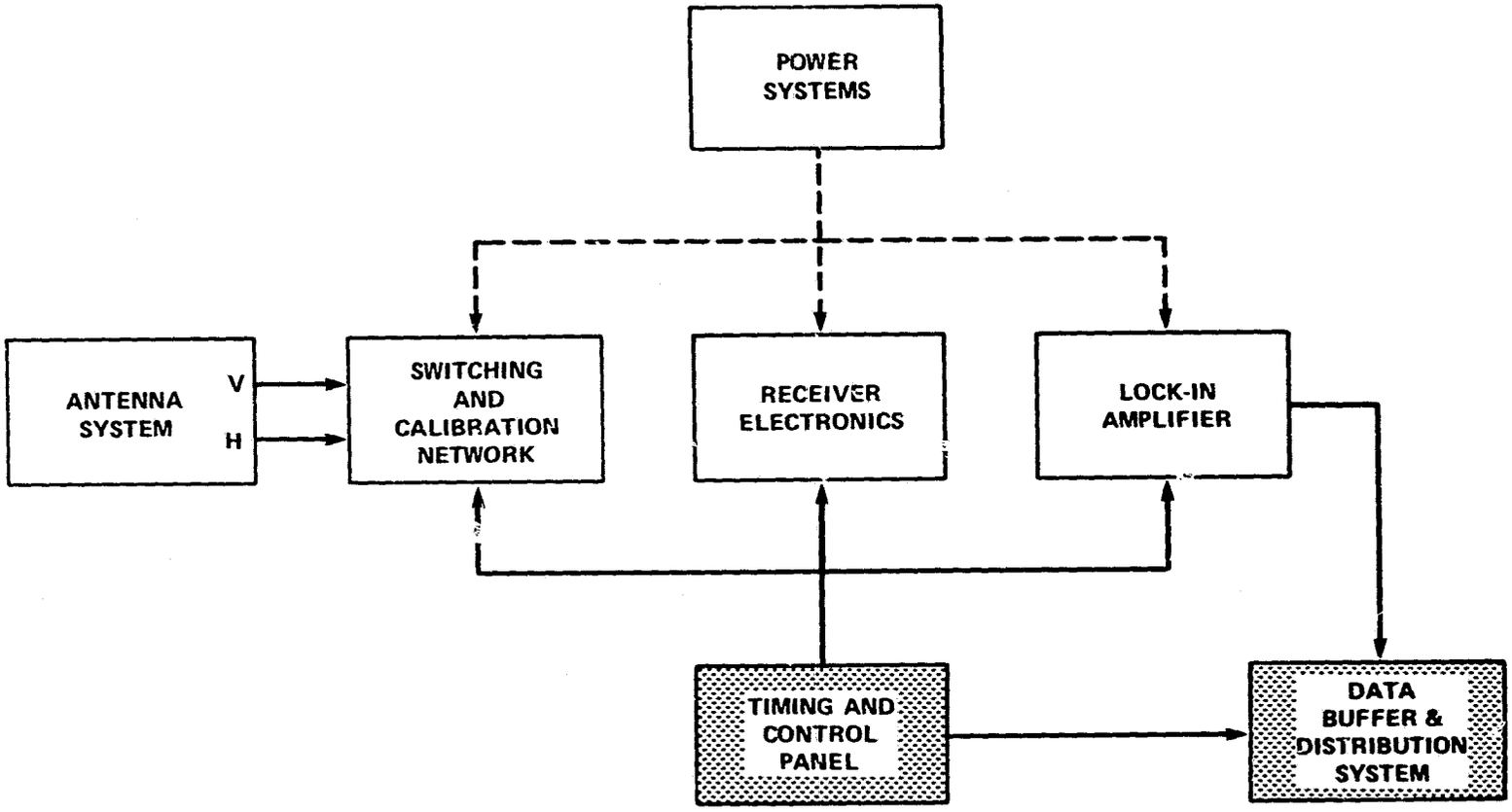

Figure 2–1. Radiometer System Block Diagram

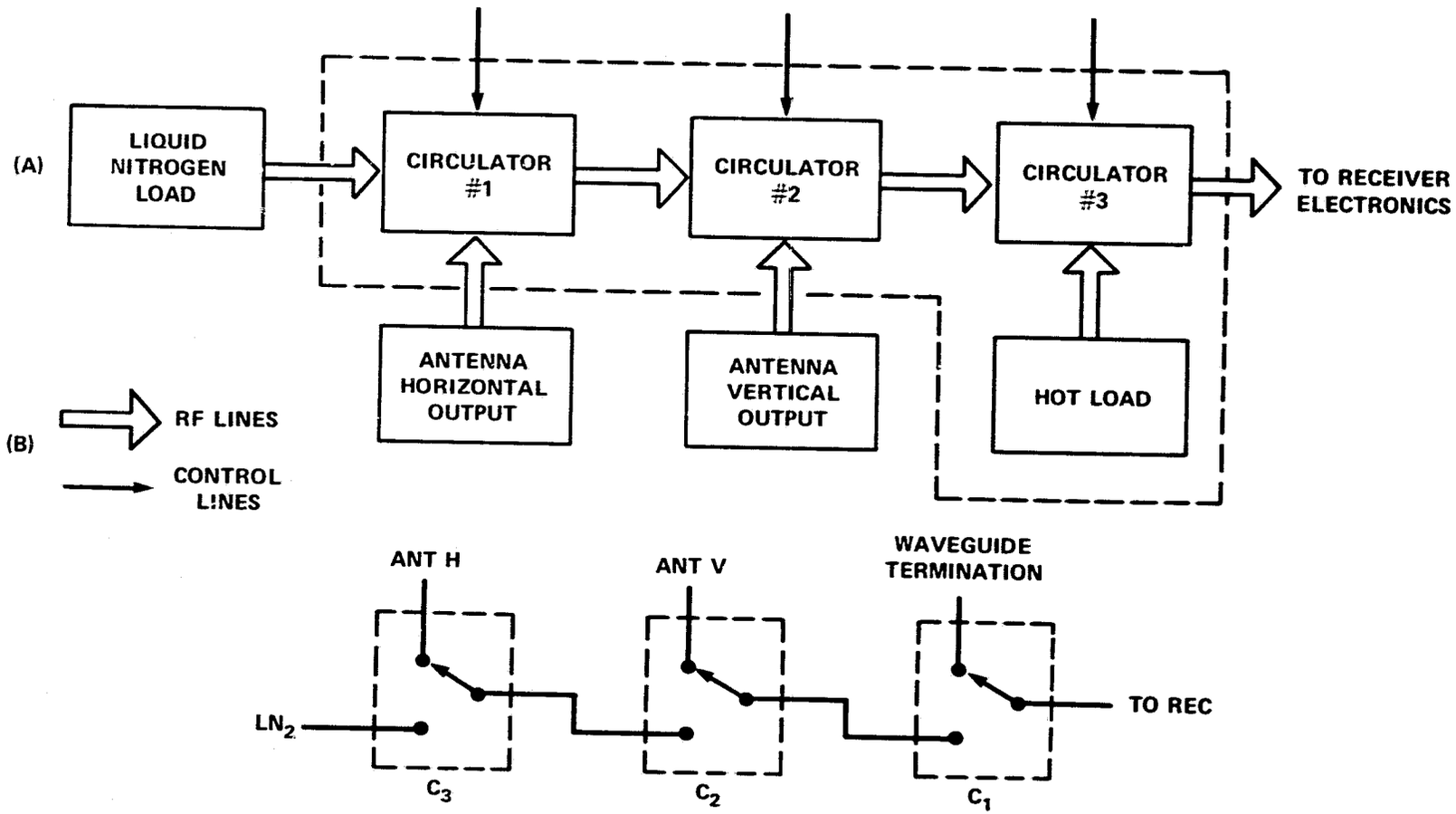

Figure 2–2. Switching and Calibration Network

2.2.2.1 Switching Block – The switching block (Figure 2-2B) is composed of latching ferrite circulators, arranged so as to provide three series-connected single-pole double-throw switches, a waveguide termination, and necessary driver circuitry. The temperature of the entire switching block is maintained at approximately 35°C. The circulator states are controlled by the timing and control system (see Section 2.2.6).

2.2.2.2 Liquid Nitron Load – The liquid nitrogen load consists of a closed cryogenic vessel and a waveguide termination immersed in a bath of LN_2.

2.2.3 Receiver Electronics

The receiver electronics converts the modulated RF signal from the SCN into a video signal which is applied to the Post Detection Processor.

2.2.4 Post Detection Processor

The post-detection processor synchronously detects the Dicke-modulated video signal and produces an output voltage of 0 to 10 volts DC. The output signal is linearly proportional to the received power, T_A, and is recorded for subsequent data reduction and analysis.

2.2.5 Power System

The power system supplies all required DC power for operation of the radiometer system.

2.2.6 Timing and Control System

The timing and control system provides the appropriate logic-control signals to the switching and calibration network. These select which radiometric measurement (cold ref., hot ref., scene vertical polarization, or scene horizontal polarization) will be processed at any one time.

3.0 BASIC RADIOMETRIC EQUATION-DERIVATION

For the SMMR, the radiometer output voltage is linearly proportional to the power of the input signal, which is produced either by a warm or cold (liquid nitrogen) reference load or by the microwave radiation incident upon the antenna.

V_A represents the output voltage in response to an input signal from the antenna of brightness temperature, T_A. Linearity of the radiometer implies

$$V_A = u + vT_A \tag{3-1a}$$

where u is a constant offset voltage, and v is a proportionality constant. Similarly, when signals are observed from the warm and cold calibration sources at the effective radiometric temperatures, T_W and T_c, respectively, the radiometer response is

$$V_W = u + vT_W \tag{3-1b}$$

and

$$V_c = u + vT_c \tag{3-1c}$$

Voltages V_A, V_W, and V_c are measurable quantities. To eliminate calibration constants u and v, it is useful to define the parameter N, refrered to as the "normalized voltage" or "normalized counts":

$$N = \frac{V_A - V_W}{V_c - V_W} \tag{3-2}$$

Substitution of Equation (3-1) into Equation (3-2) yields

$$N = \frac{(u + vT_A) - (u + vT_W)}{(u + vT_c) - (u + vT_W)} = \frac{T_A - T_W}{T_c - T_W} \tag{3-3}$$

After rearrangement, this becomes the radiometric equation

$$T_A = T_W + (T_c - T_W)\,N \tag{3-4}$$

Equation (3-4) relates the incident radiation intensity, T_A, to the observed normalized voltage, N, and two effective radiometric calibration temperatures, T_W and T_c.

This relationship is, however, incomplete in-as-much-as it does not take into account any system losses which will cause aberrations to the absolute temperatures T_A, T_W, T_c. These effects are considered in Section 4.

In Section 5, expressions formally equivalent to Equation (3-4) are derived by applying basic microwave radiative transfer theory considered in Section 4 to the SMMR collection system.

This procedure illustrates the relationships between the calibration constants, T_w and T_c, and the thermodynamic temperatures of the various components of the collection system.

4.0 SMMR SIMULATOR SYSTEM LOSSES – RADIATIVE TRANSFER ANALYSIS

4.1 Radiative Transfer Theory

This section examines the relationship between the radiation field reaching the SMMR collection system and the signal that eventually reaches the radiometer. Incident radiation does not pass unimpeded to the radiometer but is attenuated by losses in the waveguides and various switches. At the same time, thermal emissions by the lossy components contribute to the signal observed at the radiometer. The equation of microwave radiative transfer (References 39 and 40) may be used to relate the intensities of the two radiation fields as a function of the various system losses. In the following discussion, the Rayleigh-Jeans approximation to the Planck radiation law is assumed to be valid and is used throughout.

4.1.1 Radiative Transfer Theory Applied to a Cascade of Lossy Elements

Consider the transfer of radiation across a single lossy plane-parallel element, as illustrated in Figure 4-1, where the incident radiation is characterized by a brightness temperature, T_0, and the output signal by T_1. The lossy slab is at thermodynamic temperature t_1, and has an effective transmissivity, α_1.

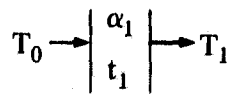

Figure 4-1. Radiative Transfer Across a Plane-Parallel Slab

The equation of radiative transfer becomes

$$T_1 = \alpha_1 T_0 + (1 - \alpha_1) t_1 \qquad (4\text{-}1)$$

The effect of an additional loss is illustrated in Figure 4.2.

The second lossy slab is at thermodynamic temperature t_2, and has an effective transmissivity, α_2.

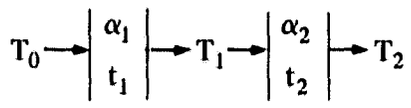

Figure 4-2. Radiative Transfer Across Two Plane-Parallel Slabs

The output signal, T_2, is

$$T_2 = \alpha_2 T_1 + (1 - \alpha_2)\, t_2 \tag{4.1-2a}$$

$$T_2 = \alpha_2 [\alpha_1 T_0 + (1 - \alpha_1)\, t_1] + (1 - \alpha_2)\, t_2 \tag{4.1-2b}$$

$$T_2 = \alpha_1 \alpha_2 T_0 + [(1 - \alpha_1)\, t_1]\, \alpha_2 + (1 - \alpha_2)\, t_2 \tag{4.1-2c}$$

The original signal, T_0, is reduced by the product of the two transmissivities, and the emission from the first lossy slab is, in turn, attenuated by the second.

If the signal T_2 now passes through a third lossy element the system becomes a cascaded triple loss as illustrated in Figure 4-3. The third lossy slab is at thermodynamic temperature, t_3 and has an effective transmissivity, α_3. The output signal, T_3, is given by

$$T_3 = \alpha_3 T_2 + (1 - \alpha_3)\, t_3 \tag{4.1-3a}$$

$$T_3 = \alpha_1 \alpha_2 \alpha_3 T_0 + [(1 - \alpha_1)\, t_1]\, \alpha_2 \alpha_3 + [(1 - \alpha_2)\, t_2]\, \alpha_3 + (1 - \alpha_3)\, t_3 \tag{4.1-3b}$$

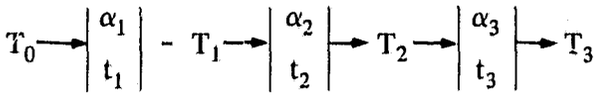

Figure 4-3. Radiative Transfer Across Three Plane-Parallel Slabs

If a cascaded triple loss system is characterized by

$$t_1 = t_2 = t_3 = t_0$$

the equation for radiative transfer becomes

$$T_3 = \alpha_3 \{\alpha_2[\alpha_1 T_0 + (1-\alpha_1)t_0] + (1-\alpha_2)t_0\} + (1-\alpha_3)t_0 \qquad (4.1\text{-}4a)$$

$$T_3 = \alpha_1\alpha_2\alpha_3 T_0 + (1-\alpha_1\alpha_2\alpha_3)\, t_0 \qquad (4.1\text{-}4b)$$

The effects of thermal losses in the SMMR simulator collection system can be calculated by repeated application of this method. The input signal at the switch block, T_{Fi}, can be computed from T_0 by applying expressions analogous to Equations (4.1-1), (4.1-2) and (4.1-3) across the entire network of losses traversed by the incident radiation. Section 4.2 develops the loss equations for the elements external to the switch block for the SMMR Simulator Radiometers.

4.1.2 Application to Cascade of Ferrite Circulator Junctions

As with the losses external to the ferrite switch block, incident radiation does not pass unimpeded through the switch block but is attenuated by losses in the various switches. The thermal emissions of the switch components also contribute to the signal received at the radiometer. The ferrite switch block used in the SMMR simulator is a cascade of two port ferrite circulators. A typical circulator, shown in Figure 4-4 consists of two input ports, T_{in1} and T_{in2}, one output port, T_{out}, and a ferrite element, F, in the center which is magnetically biased to provide direction of circulation through the junction.

If the ferrite is biased for clockwise circulation, T_{out} is proportional to T_{in1}. A term, α, defined as the direct path transmissivity relates the two signals, T_{out} and T_{in1}, as seen in Equation 4.1-5.

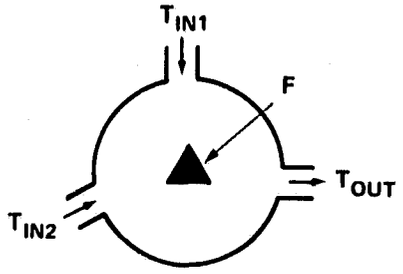

Figure 4-4. Typical Ferrite Junction-Circulator

$$T_{out} = T_{in1}\alpha + \text{an emissivity component of junction} \qquad (4.1\text{-}5)$$

A certain amount of T_{in2} leaks to the output, T_{out}, due to incomplete termination of the counter-clockwise signal path. Therefore, a fraction of T_{in2} is also found in T_{out}. A leakage term, β, defined as the indirect path transmissivity, relates T_{in2} to T_{out} in Equation (2).

$$T_{out} = T_{in2}\beta + \text{an emissivity component of junction} \qquad (4.1\text{-}6)$$

The total output can be defined as:

$$T_{out} = T_{in\,1}\,\alpha + T_{in\,2}\beta + \text{junction emissivity} \qquad (4.1\text{-}7)$$

The effective junction emissivity,

$$\text{Emissivity} = \left(1 - \sum \frac{1}{\text{junction losses}}\right) t^{\text{junction}} \qquad (4.1\text{-}8)$$

takes into account the total thermal emissivity of the junction. The losses in the junction include the direct path loss and the leakage loss. The temperature of the junction will be referred to as t_{junc}. The equation for the junction emissivity is

$$\epsilon = (1 - \alpha - \beta)\, t_{junc}. \qquad (4.1\text{-}9)$$

Therefore the complete equation for total output becomes

$$T_{out} = T_{in1}\alpha + T_{in2}\beta + (1 - \alpha - \beta)\, t_{junc}. \qquad (4.1\text{-}10)$$

Consider a double cascade of junctions where the temperatures for each junction are equal. A schematic representation of the system is shown in Figure 4-5.

Let α_{jk} be defined as the direct path transmissivity and β_{jk} be defined as the leakage loss where the subscript j refers to the junction number and k refers to the junction switch position. The junction position, k = 1 is indicative of clockwise rotation of the signal path while k = 2 indicates counter-clockwise rotation. Case 1, as shown in Figure 4-5, shall be examined in addition

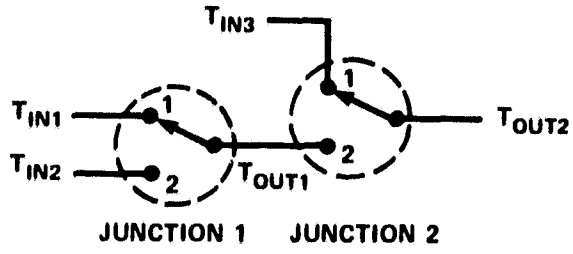

Figure 4-5. Schematic Representation
Two Junction Ferrite Switch
Configuration-Case 1

to all other cases of possible switch configurations. The equation for the output from Junction 1, T_{out1} is given as follows:

$$T_{out1} = T_{in1}\alpha_{11} + T_{in2}\beta_{11} + (1 - \alpha_{11} - \beta_{11})t \qquad (4.1\text{-}11)$$

(in which all subscripts 11 refer to the first junction being in the first switch position). The output from junction 2, T_{out2}, is seen in Equation (4.1-12)

$$T_{out2} = T_{in3}\alpha_{21} + T_{out1}\beta_{21} + (1 - \alpha_{21} - \beta_{21})t \qquad (4.1\text{-}12)$$

(The subscripts 21 indicate that the second junction is in the first switch position.) Substituting Equation (4.1-11) into Equation (4.1-12) yields the following:

$$T_{out2} = T_{in3}\alpha_{21} + [T_{in1}\alpha_{11} + T_{in2}\beta_{11} + (1 - \alpha_{11} - \beta_{11})t]\beta_{21} + (1 - \alpha_{21} - \beta_{21})t \qquad (4.1\text{-}13)$$

which reduces to:

$$T_{out2} = T_{in3}\alpha_{21} + (T_{in1}\alpha_{11} + T_{in2}\beta_{11})\beta_{21} + [1 - \alpha_{21} - (\alpha_{11} + \beta_{11})\beta_{21}]t \qquad (4.1\text{-}14)$$

Now, examine the switch configuration in Figure 4-6, in which junction 2 is now in the second switch position.

The equation for the output of the first junction is identical to the output equation of the first junction in the previous case (Recall Equation (4.1-11)).

$$T_{out1} = T_{in1}\alpha_{11} + T_{in2}\beta_{11} + (1 - \alpha_{11} - \beta_{11})t \qquad (4.1\text{-}15)$$

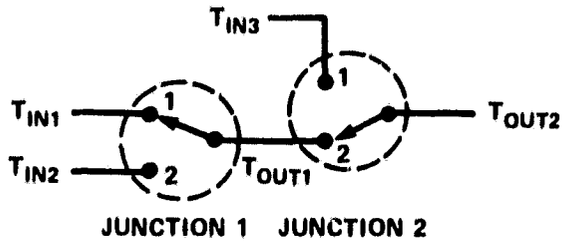

Figure 4-6. Schematic Representation
Two Junction Ferrite Switch
Configuration-Case 2

However, the equation for the output from Junction 2 for this case differs from the previous case, as seen below,

$$T_{out2} = T_{out1}\alpha_{22} + T_{in3}\beta_{22} + (1 - \alpha_{22} - \beta_{22})t \qquad (4.1\text{-}16)$$

When Equation (4.1-15) is substituted into Equation (4.1-16) one obtains the equation for T_{out2} for switch configuration 2.

$$T_{out2} = (T_{in1}\alpha_{11} + T_{in2}\beta_{11})\alpha_{22} + T_{in3}\beta_{22} + [1 - \beta_{22} - (\alpha_{11} + \beta_{11})\alpha_{22}]\,t \qquad (4.1\text{-}17)$$

The third possible switch configuration is shown in Figure 4-7.

The equation for T_{out1} is found below:

$$T_{out1} = T_{in2}\alpha_{12} + T_{in1}\beta_{12} + (1 - \alpha_{12} - \beta_{12})t \qquad (4.1\text{-}18)$$

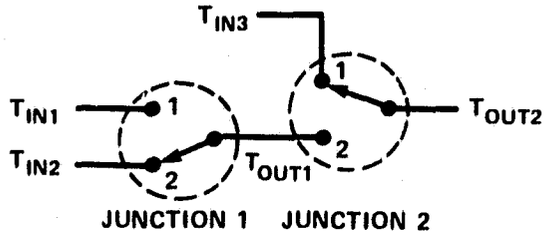

Figure 4-7. Schematic Representation
Two Junction Ferrite Switch
Configuration - Case 3

Note that the direct path loss α_{12} now is coupled with T_{in2}. The output from junction 2, T_{out2}, is defined in Equation (4.1-19)

$$T_{out2} = T_{in3}\alpha_{21} + T_{out1}\beta_{21} + (1 - \alpha_{21} - \beta_{21})t \qquad (4.1\text{-}19)$$

Substitution and reduction yield the final form of the Equation for case 3.

$$T_{out2} = (T_{in1}\beta_{12} + T_{in2}\alpha_{12})\beta_{21} + T_{in3}\alpha_{21} + [1 - \alpha_{21} - (\alpha_{12} + \beta_{12})\beta_{21}]\,t \qquad (4.1\text{-}20)$$

The final case where both junctions are in the second switch position is schematically represented in Figure 4-8.

The equation for the output of junction 1 is identical for that found in the preceeding case, and is repeated below.

$$T_{out1} = T_{in2}\alpha_{12} + T_{in1}\beta_{12} + (1 - \alpha_{12} - \beta_{12})t \qquad (4.1\text{-}21)$$

The output from junction 2, T_{out2}, for this case is defined in Equation (4.1-22)

$$T_{out2} = T_{out1}\alpha_{22} + T_{in3}\beta_{22} + (1 - \alpha_{22} - \beta_{22})t \qquad (4.1\text{-}22)$$

With the previously used methods, Equation (4.1-22) undergoes substitution and reduction to obtain a final expression for T_{out2}-case 4.

$$T_{out2} = (T_{in2}\,\alpha_{12} + T_{in1}\beta_{12})\alpha_{22} + T_{in3}\beta_{22} + [1 - \beta_{22} - (\alpha_{12} + \beta_{12})\alpha_{22}]\,t \qquad (4.1\text{-}23)$$

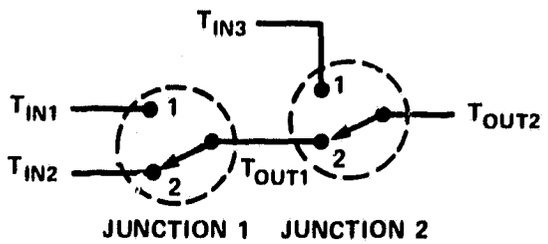

Figure 4-8. Schematic Representation
Two Junction Ferrite Switch
Configuration-Case 4

Similar expansion methods may be utilized to obtain the system output equations for tri-cascaded and quadruple cascaded ferrite switch junctions as are found in the SMMR simulator radiometers. Section 4.3 will develop the loss equations for the ferrite block for the SMMR simulator radiometers.

4.2 Losses External to the Switch Block

The losses experienced by the incident radiation external to the switch block vary according to the physical installation of the different radiometer systems in the CV-990 aircraft. Table 4-1 delineates the physical location of the radiometer system components in the CV-990.

As was noted in Section 2.2.1, the antenna system channelizes the incident radiation field so that the vertically and horizontally polarized components travel through different waveguides from the antenna system to the switch block.

For purposes of this analysis, we shall define the following terms:

1. $T_{MN} \equiv$ effective radiometric temperature
2. $\alpha_{MN} \equiv$ transmissivity of the lossy element
3. $E_{MN} \equiv$ emissivity of the lossy element $\equiv 1 - \alpha_{MN}$
4. $t_{MN} \equiv$ physical temperature of the lossy element

where the subscript M identifies a particular lossy component (Table 4-2) and N delineates the various signal paths within the system (Table 4-2, Figure 4-9 through 4-13).

Table 4-1

Radiometer System	Electronics Package	Antenna System	Waveguide Connections
6.6	Aft Cargo	Sled	Cargo, Sled
10.7	Aft Cargo	Sled	Cargo, Sled
18	Aft Cargo	Sled	Cargo, Sled
21	Cabin	Window	Cabin
21 uplook	Cabin	Window	Cabin
37	Cabin	Window	Cabin

Table 4-2

Value	M	N
0	incident radiation	common to vertical and horizontal
1	radome	warm calibration load
2	antenna	vertical polarization
3	sled waveguide	horizontal polarization
4	cargo waveguide	cold calibration load
5	cabin waveguide	uplooking channel
6	cold load waveguide	N/A
F	switch block input	N/A

If the antenna patterns have cross-polarized sidelobes, there will be a mixture of the vertically and horizontally polarized components of the incident radiation. ρ_1 is defined as the percentage of the vertically polarized radiation mixed into the horizontally polarized channel, and ρ_2 is defined similarly for the vertically polarized channel.

The sections immediately following provide a detailed description of the external loss networks for each radiometric system. In each case, equations are obtained which relate the effective brightness temperatures at the input terminal of the switch block to the various incident brightness temperatures (scene, cold load, warm load).

4.2.1 6.6GHz and 10.7GHz Radiometers

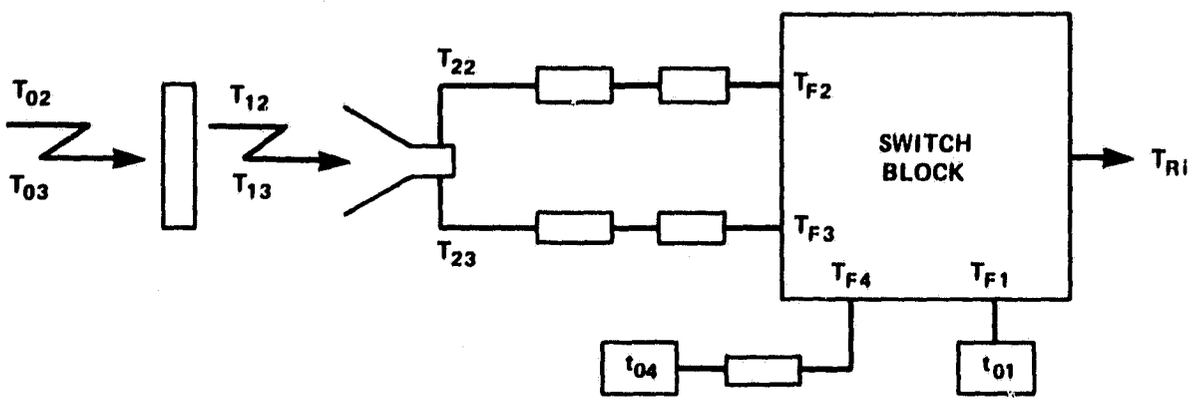

Figure 4-9

$$T_{12} = T_{02}\alpha_{12} + E_{12}t_{10} \tag{4.2-1a}$$

$$T_{13} = T_{03}\alpha_{13} + E_{13}t_{10} \tag{4.2-1b}$$

$$T_{23} = [(1-\rho_1)T_{13} + \rho_1 T_{12}]\alpha_{23} + E_{23}t_{10} \tag{4.2-2a}$$

$$T_{22} = [(1-\rho_2)T_{12} + \rho_2 T_{13}]\alpha_{22} + E_{22}t_{10} \tag{4.2-2b}$$

$$T_{F1} = t_{01} \tag{4.2-3}$$

$$T_{F2} = (T_{22}\alpha_{32} + E_{32}t_{32})\alpha_{42} + E_{42}t_{42} \tag{4.2-4}$$

$$T_{F3} = (T_{23}\alpha_{33} + E_{33}t_{33})\alpha_{43} + E_{43}t_{43} \tag{4.2-5}$$

$$T_{F4} = t_{04}\alpha_{60} + E_{60}t_{60} \tag{4.2-6}$$

4.2.2 18GHz Radiometer

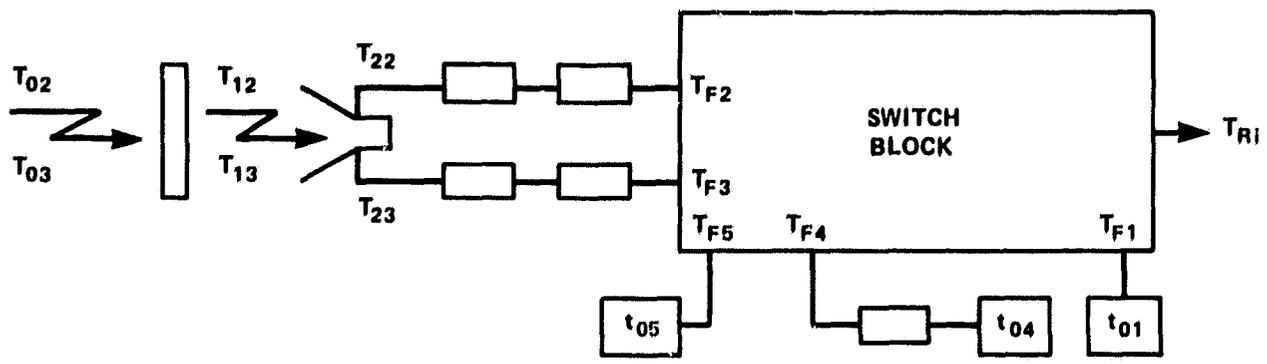

Figure 4-10

Note: 1. t_{05} ⇒ physical temperature of a termination

2. $t_{05} = t_{01}$

Loss term equations for the 18GHz radiometer are identical to the equations for the 6.6GHz and 10.7GHz radiometers (Eqs. (4.2-1) through (4.2-6)).

One additional equation is required

$$T_{F5} = t_{05} = t_{01} \tag{4.2-7}$$

4.2.3 21GHz Radiometer

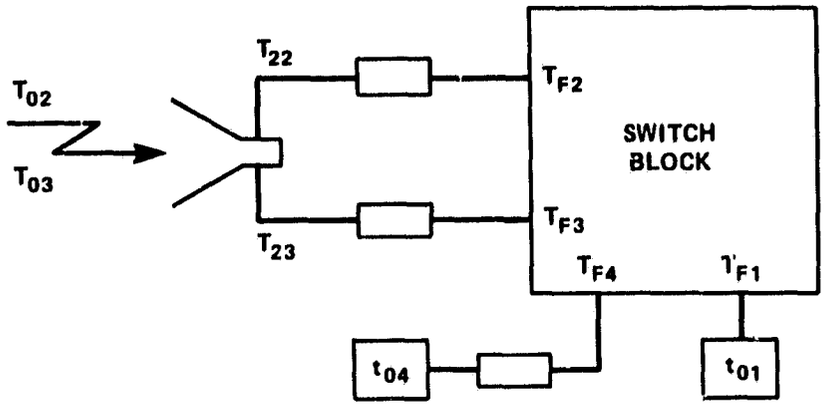

Figure 4-11

$$T_{23} = [(1-\rho_1)T_{03} + \rho_1 T_{02}]\alpha_{23} + E_{23}t_{10} \tag{4.2-8a}$$

$$T_{22} = [(1-\rho_2)T_{02} + \rho_2 T_{03}]\alpha_{22} + E_{22}t_{10} \tag{4.2-8b}$$

T_{F1} see Equation (4.2-3)

$$T_{F2} = T_{22}\alpha_{52} + E_{52}t_{52} \tag{4.2-9}$$

$$T_{F3} = T_{23}\alpha_{53} + E_{53}t_{53} \tag{4.2-10}$$

T_{F4} see Equation (4.2-6)

4.2.4 21GHz Uplook Radiometer

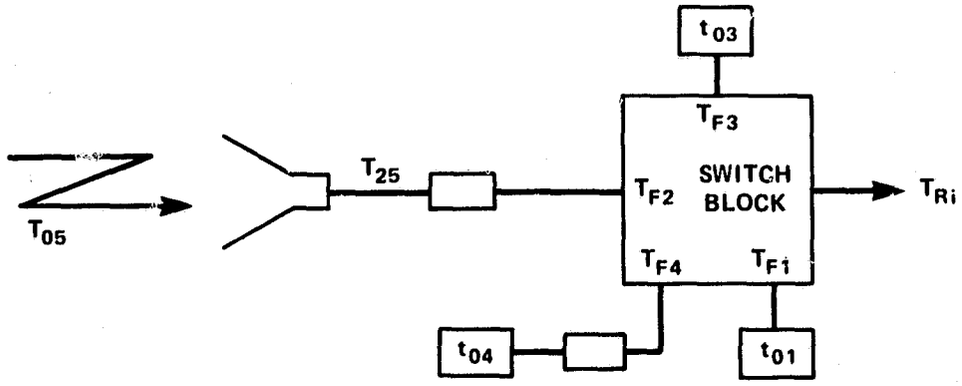

Figure 4-12

Note: 1. $t_{03} \Rightarrow$ physical temperature of a termination, $t_{03} = t_{01}$

2. Uplook channel for 21 GHz uses the vertical channel switch block input port

$$T_{25} = T_{05}\alpha_{25} + E_{25}t_{25} \qquad (4.2\text{-}11)$$

T_{F1} see Equation (4.2-3)

$$T_{F2} = T_{25}\alpha_{55} + E_{55}t_{55} \qquad (4.2\text{-}12)$$

$$T_{F3} = t_{01} \qquad (4.2\text{-}13)$$

T_{F4} see Equation (4.2-6)

4.2.5 37 GHz Radiometer

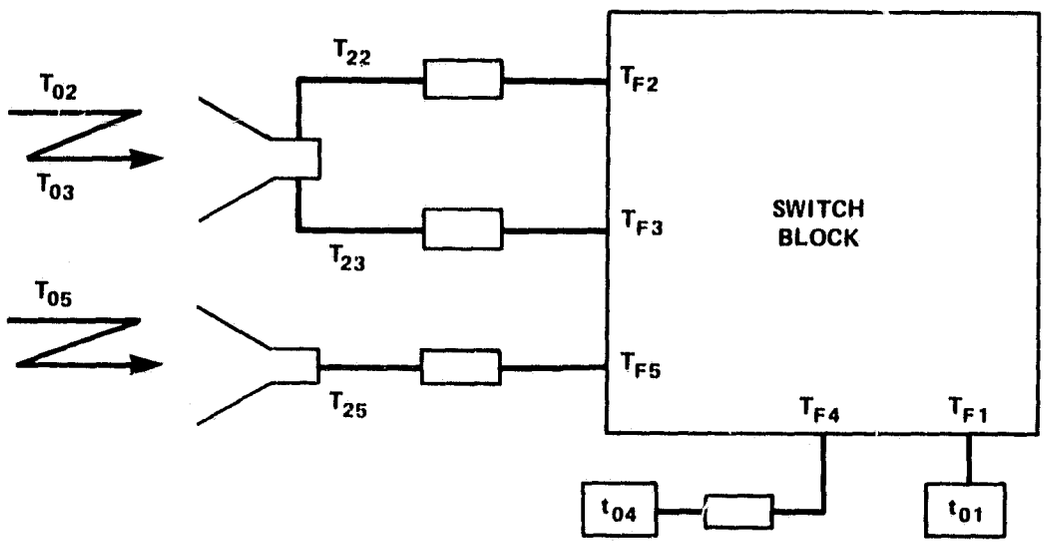

Figure 4-13

$T_{25} \Rightarrow$ see Equation (4.2-8a)

$T_{22} \Rightarrow$ see Equation (4.2-8b)

$T_{25} \Rightarrow$ see Equation (4.2-11)

$T_{F1} \Rightarrow$ see Equation (4.2-3)

$T_{F2} \Rightarrow$ see Equation (4.2-9)

$$T_{F3} \Rightarrow \text{see Equation (4.2-10)}$$

$$T_{F4} \Rightarrow \text{see Equation (4.2-6)}$$

$$T_{F5} = T_{25}\alpha_{55} + E_{55}t_{55} \qquad (4.2\text{-}14)$$

4.3 Losses Internal to the Switch Block

Two different switch block configurations occur in the various SMMR simulator radiometers. The switch blocks consist of a cascade of ferrite circulator junctions. The 6.6, 10.7, 21, and 21 GHz uplook radiometers use a cascade of three junctions, while the 18 and 37 GHz radiometers have a four junction cascade. A set of equations is derived for each switch block configuration.

For purposes of this analysis the following terms are defined:

1. $T_{Fi} \equiv$ effective radiometric temperature at the input to the switch block
2. $T_{Ri} \equiv$ effective radiometric temperature at the output of the switch block
3. $\alpha_{jk} \equiv$ transmissivity of the junction
4. $E_{jk} \equiv$ emissivity of the junction
5. $\beta_{jk} \equiv$ isolation of the junction

where i = 1 = warm calibration load

2 = vertical polarization of incident radiation

3 = horizontal polarization of incident radiation

4 = cold calibration load

5 = uplooking channel

j ≡ switch number

k = 1 ≡ schematic switch position representation of CW circulation

2 ≡ schematic switch position representation of CCW circulation

The analysis of the switch block takes two approaches. The first approach considers every circulator junction individually using the terms previously defined. The second approach considers only those parameters physically measurable. This is required since some circulator junction

ports are internal of the switch block and thus inaccessable. The final results of the two approaches are equivalent.

To facilitate the second approach additional terms are defined:

1. $A_{MN} \equiv$ measurable path loss
2. $B_{MN} \equiv$ measurable path isolation
3. $\epsilon_N \equiv$ switch block emissivity

where M ≡ input (i) contributing the signal

N ≡ switch setting for primary input signal path

4.3.1 Switch Block 6.6, 10.7, 21, 21 Uplook

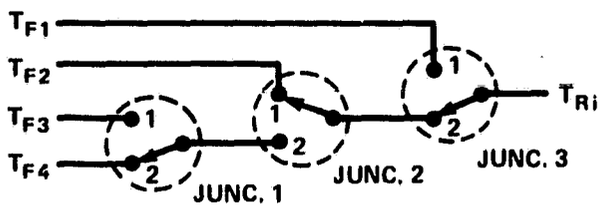

Figure 4-14. Schematic Representation Switch Block 6.6, 10.7, 21, 21 GHz Uplook

Analysis of the switch block for the 6.6, 10.7, 21, and 21 GHz uplook radiometers (Figure 4-14) in each of the four measurement configurations (T_{R1}, T_{R2}, T_{R3}, T_{R4}) yields the set of equations given below in matrix notation where $t_0 \equiv$ physical temperature of the switch block.

$$\begin{bmatrix} T_{R1} \\ T_{R2} \\ T_{R3} \\ T_{R4} \end{bmatrix} = \begin{bmatrix} \alpha_{31} & \beta_{22}\beta_{31} & \beta_{12}\alpha_{22}\beta_{31} & \alpha_{12}\alpha_{22}\beta_{31} \\ \beta_{32} & \alpha_{21}\alpha_{32} & \beta_{12}\beta_{21}\alpha_{32} & \alpha_{12}\beta_{21}\alpha_{32} \\ \beta_{32} & \beta_{22}\alpha_{32} & \alpha_{11}\alpha_{22}\alpha_{32} & \beta_{11}\alpha_{22}\alpha_{32} \\ \beta_{32} & \beta_{22}\alpha_{32} & \beta_{12}\alpha_{22}\alpha_{32} & \alpha_{12}\alpha_{22}\alpha_{32} \end{bmatrix} \begin{bmatrix} T_{F1} \\ T_{F2} \\ T_{F3} \\ T_{F4} \end{bmatrix} + \begin{bmatrix} E_{12}\alpha_{22}\beta_{31} + E_{22}\beta_{31} + E_{31} \\ E_{12}\beta_{21}\alpha_{32} + E_{21}\alpha_{32} + E_{32} \\ E_{11}\alpha_{22}\alpha_{32} + E_{22}\alpha_{32} + E_{32} \\ E_{12}\alpha_{22}\alpha_{32} + E_{22}\alpha_{32} + E_{32} \end{bmatrix} t_0 \quad (4\text{-M1})$$

The matrix Equation (4-M1) is generated in terms of the individual switch characteristics. Since these are not separately measurable as noted above, the matrix equation is rewritten in terms of measurable quantities.

$$\begin{bmatrix} T_{R1} \\ T_{R2} \\ T_{R3} \\ T_{R4} \end{bmatrix} = \begin{bmatrix} A_{11} & B_{21} & B_{31} & B_{41} \\ B_{12} & A_{22} & B_{32} & B_{42} \\ B_{13} & B_{23} & A_{33} & B_{43} \\ B_{14} & B_{24} & B_{34} & A_{44} \end{bmatrix} \begin{bmatrix} T_{F1} \\ T_{F2} \\ T_{F3} \\ T_{F4} \end{bmatrix} + \begin{bmatrix} \epsilon_1 \\ \epsilon_2 \\ \epsilon_3 \\ \epsilon_4 \end{bmatrix} t_0 \qquad (4\text{-M2})$$

The matrices and vectors in Equations (4-M1) and (4-M2) are equivalent term for term. Examination of the switch configurations and the term equivalency equations for (4-M1) and (4-M2), yields the following simplification:

1. $B_{12} = B_{13} = B_{14}$ define as B_1

and 2. $B_{23} = B_{24}$ define as B_2

Equivalence of the two emissivity vectors yields the following where each effective emissivity is expressed in terms of the measurable characteristics A_{MN} and B_{MN}

$$\epsilon_1 = 1 - A_{11} - B_{21} - B_{31} - B_{41} \qquad (4.3\text{-}1)$$

$$\epsilon_2 = 1 - A_{22} - B_1 - B_{32} - B_{42} \qquad (4.3\text{-}2)$$

$$\epsilon_3 = 1 - A_{33} - B_1 - B_2 - B_{43} \qquad (4.3\text{-}3)$$

$$\epsilon_4 = 1 - A_{44} - B_1 - B_2 - B_{34} \qquad (4.3\text{-}4)$$

The final form of the switch block loss equation for the 6.6, 10.7 and 21 and 21 GHz uplook radiometer systems can thus be written as follows:

$$\begin{bmatrix} T_{R1} \\ T_{R2} \\ T_{R3} \\ T_{R4} \end{bmatrix} = \begin{bmatrix} A_{11} & B_{21} & B_{31} & B_{41} \\ B_1 & A_{22} & B_{32} & B_{42} \\ B_1 & B_2 & A_{33} & B_{43} \\ B_1 & B_2 & B_{34} & A_{44} \end{bmatrix} \begin{bmatrix} T_{F1} \\ T_{F2} \\ T_{F3} \\ T_{F4} \end{bmatrix} + \begin{bmatrix} 1 - A_{11} - B_{21} - B_{31} - B_{41} \\ 1 - B_1 - A_{22} - B_{32} - B_{42} \\ 1 - B_1 - B_2 - A_{33} - B_{43} \\ 1 - B_1 - B_2 - B_{34} - A_{44} \end{bmatrix} t_0 \qquad (4\text{-M3})$$

4.3.2 Switch Block 18 and 37 GHz

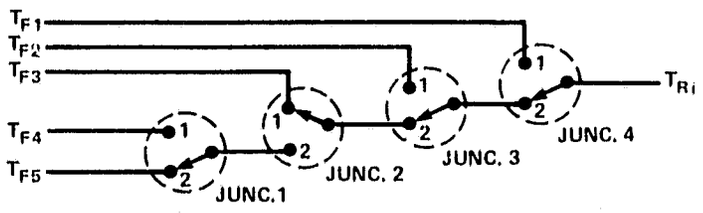

Figure 4-15. Schematic Representation Switch Block for 18 and 37 GHz

Analysis of the switch block for the 18 and 37 GHz radiometer systems, Figure 4-15, gives the equation set (4-M4) shown below, in terms of the individual switch characteristics.

$$\begin{bmatrix} T_{R1} \\ T_{R2} \\ T_{R3} \\ T_{R4} \\ T_{R5} \end{bmatrix} = \begin{bmatrix} \alpha_{41} & \beta_{32}\beta_{41} & \beta_{22}\alpha_{32}\beta_{41} & \alpha_{11}\alpha_{22}\alpha_{32}\beta_{41} & \beta_{11}\alpha_{22}\alpha_{32}\beta_{41} \\ \beta_{42} & \alpha_{31}\alpha_{42} & \beta_{22}\beta_{31}\alpha_{42} & \alpha_{11}\alpha_{22}\beta_{31}\alpha_{42} & \beta_{11}\alpha_{22}\beta_{31}\alpha_{42} \\ \beta_{42} & \beta_{32}\alpha_{42} & \alpha_{21}\alpha_{32}\alpha_{42} & \alpha_{11}\beta_{21}\alpha_{32}\alpha_{42} & \beta_{11}\beta_{21}\alpha_{32}\alpha_{42} \\ \beta_{42} & \beta_{32}\alpha_{42} & \beta_{22}\alpha_{32}\alpha_{42} & \alpha_{11}\alpha_{22}\alpha_{32}\alpha_{42} & \beta_{11}\alpha_{22}\alpha_{32}\alpha_{42} \\ \beta_{42} & \beta_{32}\alpha_{42} & \beta_{22}\alpha_{32}\alpha_{42} & \beta_{12}\alpha_{22}\alpha_{32}\alpha_{42} & \alpha_{12}\alpha_{22}\alpha_{32}\alpha_{42} \end{bmatrix} \begin{bmatrix} T_{F1} \\ T_{F2} \\ T_{F3} \\ T_{F4} \\ T_{F5} \end{bmatrix} + \begin{bmatrix} E_{11}\alpha_{22}\alpha_{32}\beta_{41} + E_{22}\alpha_{32}\beta_{41} + E_{32}\beta_{41} + E_{41} \\ E_{11}\alpha_{22}\beta_{31}\alpha_{42} + E_{22}\beta_{31}\alpha_{42} + E_{31}\alpha_{42} + E_{42} \\ E_{11}\beta_{21}\alpha_{32}\alpha_{42} + E_{21}\alpha_{32}\alpha_{42} + E_{32}\alpha_{42} + E_{42} \\ E_{11}\alpha_{22}\alpha_{32}\alpha_{42} + E_{22}\alpha_{32}\alpha_{42} + E_{32}\alpha_{42} + E_{42} \\ E_{11}\alpha_{22}\alpha_{32}\alpha_{42} + E_{22}\alpha_{32}\alpha_{42} + E_{32}\alpha_{42} + E_{42} \end{bmatrix} t_0 \quad \text{(4-M4)}$$

When rewritten in terms of physically measurable switch block characteristics, the equation set becomes

$$\begin{bmatrix} T_{R1} \\ T_{R2} \\ T_{R3} \\ T_{R4} \\ T_{R5} \end{bmatrix} = \begin{bmatrix} A_{11} & B_{21} & B_{31} & B_{41} & B_{51} \\ B_{12} & A_{22} & B_{32} & B_{42} & B_{52} \\ B_{13} & B_{23} & A_{33} & B_{43} & B_{53} \\ B_{14} & B_{24} & B_{34} & A_{44} & B_{54} \\ B_{15} & B_{25} & B_{35} & B_{45} & A_{55} \end{bmatrix} \begin{bmatrix} T_{F1} \\ T_{F2} \\ T_{F3} \\ T_{F4} \\ T_{F5} \end{bmatrix} + \begin{bmatrix} \epsilon_1 \\ \epsilon_2 \\ \epsilon_3 \\ \epsilon_4 \\ \epsilon_5 \end{bmatrix} \quad \text{(4-M5)}$$

Examination of the term equivalency equations shows that

$$B_{12} = B_{13} = B_{14} = B_{15} \qquad \text{define as } B_1$$

$$B_{23} = B_{24} = B_{25} \qquad \text{define as } B_2$$

$$\text{and } B_{34} = B_{35} \qquad \text{define as } B_3$$

The final form of the switch-loss equation for the 18 and 37 GHz radiometers in terms of measurable quantities is Equation (4-M6):

$$\begin{bmatrix} T_{R1} \\ T_{R2} \\ T_{R3} \\ T_{R4} \\ T_{R5} \end{bmatrix} = \begin{bmatrix} A_{11} & B_{21} & B_{31} & B_{41} & B_{51} \\ B_1 & A_{22} & B_{32} & B_{42} & B_{52} \\ B_1 & B_2 & A_{33} & B_{43} & B_{53} \\ B_1 & B_2 & B_3 & A_{44} & B_{54} \\ B_1 & B_2 & B_3 & B_{45} & A_{55} \end{bmatrix} \begin{bmatrix} T_{F1} \\ T_{F2} \\ T_{F3} \\ T_{F4} \\ T_{F5} \end{bmatrix} + \begin{bmatrix} 1 - A_{11} - B_{21} - B_{31} - B_{41} - B_{51} \\ 1 - A_{22} - B_1 - B_{32} - B_{42} - B_{52} \\ 1 - B_1 - B_2 - A_{33} - B_{43} - B_{53} \\ 1 - B_1 - B_2 - B_3 - A_{44} - B_{54} \\ 1 - B_1 - B_2 - B_3 - B_{45} - A_{55} \end{bmatrix} t_0 \quad \text{(4-M6)}$$

5.0 SMMR SIMULATOR RADIOMETER EQUATIONS

In Section 4, sets of equations were developed for each radiometer which describe the effects of thermal losses, switch leakages, and polarization mixings on the different incident signals (scene, warm load, cold load). In this section each set of equations is combined to obtain an expression for the absolute brightness temperature of the incident scene radiation.

5.1 Derivation Method

Recall the basic radiometric equation derived in Section 3:

$$T_A = T_W + (T_c - T_W)N \tag{5-1}$$

where

$$N = \frac{V_A - V_W}{V_c - V_W} \tag{5-2}$$

Three analogous equation sets may be written for the SMMR simulator radiometers:

$$T_{R2} = T_{R1} + (T_{R4} - T_{R1})N_2 \tag{5-3a}$$

where

$$N_2 = \frac{V_2 - V_1}{V_4 - V_1} \tag{5-3b}$$

$$T_{R3} = T_{R1} + (T_{R4} - T_{R1})N_3 \tag{5-4a}$$

where

$$N_3 = \frac{V_3 - V_1}{V_4 - V_1} \tag{5-4b}$$

and

$$T_{R5} = T_{R1} - (T_{R4} - T_{R1})N_5 \tag{5-5a}$$

where

$$N_5 = \frac{V_5 - V_1}{V_4 - V_1} \tag{5-5b}$$

where 1 = warm calibration load

2 = vertical component of signal

3 = horizontal component of signal

4 = cold calibration load

5 = uplooking signal

The incident scene brightness temperatures are obtained by substituting expressions for T_{Ri} derived in Section 4 into Equations (5-3a), (5-4a) and (5-5a). For the 6.6, 10.7, 18, and 21 GHz radiometers, T_{R2} and T_{R3} contain mixtures of the horizontally and vertically polarized incident signals. Thus Equations (5-3a) and (5-3b) must be solved simultaneously to yield separate expressions for the differently polarized signals T_{02} and T_{03}. For the 37 GHz radiometer, mixtures of three states (horizontal, vetrical, uplook) are obtained and three equations must be solved simultaneously for T_{02}, T_{03} and T_{05}. The details of these laborious derivations are presented in Reference 42; the results are presented below.

5.2 Radiometric Equations

This section tabulates the various radiometeric equations for SMMR simulator.

Note: a_{MN}, E_{MN}, and t_{MN} as defined in section 4.2; A_{MN}, B_{MN}, and ϵ_N as defined in section 4.3.

5.2.1 6.6 and 10.7GHz Radiometer Systems

$$T_{02} = t_{01}\left[\frac{B_2C_1 - B_1C_2}{A_1B_2 - A_2B_1}\right] + t_{04}\left[\frac{B_2D_1 - B_1D_2}{A_1B_2 - A_2B_1}\right] + \left[\frac{B_2E_1 - B_1E_2}{A_1B_2 - A_2B_1}\right]$$

$$T_{03} = t_{01}\left[\frac{A_1C_2 - C_1A_2}{A_1B_2 - A_2B_1}\right] + t_{04}\left[\frac{A_1D_2 - A_2D_1}{A_1B_2 - A_2B_1}\right] + \left[\frac{A_1E_2 - E_1A_2}{A_1B_2 - A_2B_1}\right]$$

where:

$$A_1 = a_1\rho_1\alpha_{12}\alpha_{23}\alpha_{33}\alpha_{43} + b_1(1-\rho_2)\alpha_{12}\alpha_{22}\alpha_{32}\alpha_{42}$$

$$A_2 = a_2\rho_1\alpha_{12}\alpha_{23}\alpha_{33}\alpha_{43} + b_2(1-\rho_2)\alpha_{12}\alpha_{22}\alpha_{32}\alpha_{42}$$

$$B_1 = a_1(1-\rho_1)\alpha_{13}\alpha_{23}\alpha_{33}\alpha_{43} + b_1\rho_2\alpha_{13}\alpha_{22}\alpha_{32}\alpha_{42}$$

$$B_2 = a_2(1-\rho_1)\alpha_{13}\alpha_{23}\alpha_{33}\alpha_{43} + b_2\rho_2\alpha_{13}\alpha_{22}\alpha_{32}\alpha_{42}$$

$$C_1 = c_1 + e_1$$

$$C_2 = c_2 + e_2$$

$$D_1 = d_1 \alpha_{60}$$

$$D_2 = d_2 \alpha_{60}$$

$$E_1 = d_1 E_{60} t_{60} - b_1 [E_{32} t_{32} \alpha_{42} + E_{42} t_{42} + E_{22} t_2 \alpha_{32} \alpha_{42} + E_{13} t_1 \rho_2 \alpha_{22} \alpha_{32} \alpha_{42} + E_{12} t_1 (1 - \rho_2) \alpha_{22} \alpha_{32} \alpha_{42}] - a_1 [E_{33} t_{33} \alpha_{43} + E_{43} t_{43} + \alpha_{33} \alpha_{43} E_{23} t_2 + E_{13} t_1 (1 - \rho_1) \alpha_{33} \alpha_{23} \alpha_{43} + E_{12} t_1 \rho_1 \alpha_{23} \alpha_{33} \alpha_{43}]$$

$$E_2 = d_2 E_{60} t_{60} - b_2 [E_{32} t_{32} \alpha_{42} + E_{42} t_{42} + E_{22} t_2 \alpha_{32} \alpha_{42} + E_{13} t_1 \rho_2 \alpha_{22} \alpha_{32} \alpha_{42} + E_{12} t_1 (1 - \rho_2) \alpha_{22} \alpha_{32} \alpha_{42}] - a_2 [E_{33} t_{33} \alpha_{43} + E_{43} t_{43} + \alpha_{33} \alpha_{43} E_{23} t_2 + E_{13} t_1 (1 - \rho_1) \alpha_{33} \alpha_{32} \alpha_{43} + E_{12} t_1 \rho_1 \alpha_{23} \alpha_{33} \alpha_{43}]$$

$$a_1 = A_{33} - B_{31} + N_{II}(B_{31} - B_{34})$$

$$a_2 = B_{32} - B_{31} + N_V(B_{31} - B_{34})$$

$$b_1 = B_2 - B_{21} + N_{II}(B_{21} - B_2)$$

$$b_2 = A_{22} - B_{21} + N_V(B_{21} - B_2)$$

$$c_1 = A_{11} - B_1 + N_{II}(B_1 - A_{11})$$

$$c_2 = A_{11} - B_1 + N_V(B_1 - A_{11})$$

$$d_1 = B_{41} - B_{43} + N_{II}(A_{44} - B_{41})$$

$$d_2 = B_{41} - B_{42} + N_V(A_{44} - B_{41})$$

$$e_1 = \epsilon_1 - \epsilon_3 + N_{II}(\epsilon_4 - \epsilon_1)$$

$$e_2 = \epsilon_1 - \epsilon_2 + N_V(\epsilon_4 - \epsilon_1)$$

5.2.2 18GHz Radiometers

$$T_{02} = t_{01}\left[\frac{B_2C_1 - B_1C_2}{A_1B_2 - A_2B_1}\right] + t_{04}\left[\frac{B_2D_1 - B_1D_2}{A_1B_2 - A_2B_1}\right] + \left[\frac{B_2E_1 - B_1E_2}{A_1B_2 - A_2B_1}\right]$$

$$T_{03} = t_{01}\left[\frac{A_1C_2 - A_2C_1}{A_1B_2 - A_2B_1}\right] + t_{04}\left[\frac{A_1D_2 - A_2D_1}{A_1B_2 - A_2B_1}\right] + \left[\frac{A_1E_2 - A_2E_1}{A_1B_2 - A_2B_1}\right]$$

where:

$$A_1 = a_1 \rho_1 \alpha_{12} \alpha_{33} \alpha_{43} \alpha_{23} + b_1 (1 - \rho_2) \alpha_{12} \alpha_{22} \alpha_{32} \alpha_{42}$$

$$A_2 = a_2 \rho_1 \alpha_{12} \alpha_{33} \alpha_{43} \alpha_{23} + b_2 (1 - \rho_2) \alpha_{12} \alpha_{22} \alpha_{32} \alpha_{42}$$

$$B_1 = a_1(1-\rho_1)\alpha_{13}\alpha_{23}\alpha_{33}\alpha_{43} + b_1\rho_2\alpha_{13}\alpha_{22}\alpha_{32}\alpha_{42}$$

$$B_2 = a_2(1-\rho_1)\alpha_{13}\alpha_{23}\alpha_{33}\alpha_{43} + b_2\rho_2\alpha_{13}\alpha_{22}\alpha_{32}\alpha_{42}$$

} same as 6.6/10.7

$$C_1 = c_1 + e_1 + f_1$$

$$C_2 = c_2 + e_2 + f_2$$

$D_1 \Rightarrow$ same as 6.6/10.7

$D_2 \Rightarrow$ same as 6.6/10.7

$E_1 \Rightarrow$ same as 6.6/10.7

$E_2 \Rightarrow$ same as 6.6/10.7

$$a_1 = A_{33} - B_{31} + N_H(B_{31} - B_3)$$

$$a_2 = B_{32} - B_{31} + N_V(B_{31} - B_3)$$

$$b_1 = B_2 - B_{21} + N_H(B_{21} - B_2)$$

$$b_2 = A_{22} - B_{21} + N_V(B_{21} - B_2)$$

$$c_1 = A_{11} - B_{12} + N_H(B_{12} - A_{11})$$

$$c_2 = A_{11} - B_{12} + N_V(B_{12} - A_{11})$$

$$d_1 = B_{41} - B_{43} + N_H(A_{44} - B_{41})$$

$$d_2 = B_{41} - B_{42} + N_V(A_{44} - B_{41})$$

$$e_1 = B_{51} - B_{53} + N_H(B_{54} - B_{51})$$

$$e_2 = B_{51} - B_{52} + N_V(B_{54} - B_{51})$$

$$f_1 = \epsilon_1 - \epsilon_3 + N_H(\epsilon_4 - \epsilon_1)$$

$$f_2 = \epsilon_1 - \epsilon_2 + N_V(\epsilon_4 - \epsilon_1)$$

5.2.3 21 GHz Radiometer

$$T_{02} = t_{01}\left[\frac{B_2C_1 - B_1C_2}{A_1B_2 - A_2B_1}\right] + t_{04}\left[\frac{B_2D_1 - B_1D_2}{A_1B_2 - A_2B_1}\right] + \left[\frac{B_2E_1 - B_1E_2}{A_1B_2 - A_2B_1}\right]$$

$$T_{03} = t_{01}\left[\frac{A_1C_2 - A_2C_1}{A_1B_2 - A_2B_1}\right] + t_{04}\left[\frac{A_1D_2 - A_2D_1}{A_1B_2 - A_2B_1}\right] + \left[\frac{A_1E_2 - A_2E_1}{A_1B_2 - A_2B_1}\right]$$

where:

$$A_1 = a_1\rho_1\alpha_{23}\alpha_{53} + b_1(1-\rho_2)\alpha_{22}\alpha_{52}$$

$$A_2 = a_2\rho_1\alpha_{23}\alpha_{53} + b_2(1-\rho_2)\alpha_{22}\alpha_{52}$$

$$B_1 = a_1(1-\rho_1)\alpha_{23}\alpha_{53} + b_1\rho_2\alpha_{22}\alpha_{52}$$

$$B_2 = a_2(1-\rho_1)\alpha_{23}\alpha_{53} + b_2\rho_2\alpha_{22}\alpha_{52}$$

$$C_1 = c_1 + e_1$$

$$C_2 = c_2 + e_2$$

D_1 = same as 6.6/10.7

D_2 = same as 6.6/10.7

$$E_1 = d_1 E_{60} t_{60} - b_1 (E_{22} t_2 \alpha_{52} + E_{52} t_{52}) - a_1 (E_{23} t_2 \alpha_{53} + E_{53} t_{53})$$

$$E_2 = d_2 E_{60} t_{60} - b_2 (E_{22} t_2 \alpha_{52} + E_{52} t_{52}) - a_2 (E_{23} t_2 \alpha_{53} + E_{53} t_{53})$$

$$a_1 = A_{33} - B_{31} + N_H (B_{31} - B_{34})$$

$$a_2 = B_{32} - B_{31} + N_V (B_{31} - B_{34})$$

$$b_1 = B_2 - B_{21} + N_H (B_{21} - B_2)$$

$$b_2 = A_{22} - B_{21} + N_V (B_{21} - B_2)$$

$$c_1 = A_{11} - B_1 + N_H (B_1 - A_{11})$$

$$c_2 = A_{11} - B_1 + N_V (B_1 - A_{11})$$

$$d_1 = B_{41} - B_{43} + N_H (A_{44} - B_{41})$$

$$d_2 = B_{41} - B_{42} + N_V (A_{44} - B_{41})$$

$$e_1 = \epsilon_1 - \epsilon_3 + N_H (\epsilon_4 - \epsilon_1)$$

$$e_2 = \epsilon_1 - \epsilon_2 + N_V (\epsilon_4 - \epsilon_1)$$

5.2.4 21 GHz Uplook Radiometer

$$T_{05} = At_{01} + Bt_{01} N + Ct_{04} + Dt_{04} N + EN + F + G + H$$

where:

$$A = \{1 + B_{31} - \epsilon_2 - B_1 B_{32}\} \div I$$

$$B = \{-1 - B_{31} + \epsilon_4 + B_1 + B_{34}\} \div I$$

$$C = \{\alpha_{60} [B_{41} - \alpha_{60}]\} \div I$$

$$D = \{\alpha_{60} [\alpha_{60} - B_{41}]\} \div I$$

$$E = \{E_{60} t_{60} [B_{41} + A_{44}] + E_{55} t_{55} [B_2 - B_1] + E_{25} t_{25} [B_1 \alpha_{55} \alpha_{25} - B_2 \alpha_{55} \alpha_{25}]\} \div I$$

$$F = \{E_{60} t_{60} [B_{41} - B_{42}]\} \div I$$

$$G = \{E_{55}\, t_{55}\, [B_{21} - A_{22}]\} \div I$$

$$H = \{E_{25}\, t_{25}\, [\alpha_{25}\alpha_{55}(A_{22} - B_{21})]\} \div I$$

$$I = [\alpha_{55}A_{22} - (B_{21}\alpha_{55})(1 - N) - B_2\alpha_{55}N]$$

5.2.5 37 GHz Radiometer

$$\begin{aligned} T_{05} = \{ & t_{04}[R_1(Y_2Z_3 - Y_3Z_2) - S_1(Y_1Z_3 - Y_3Z_1) + U_1(Y_1Z_2 - Y_2Z_1)] \\ & + t_{01}[R_2(Y_2Z_3 - Y_3Z_2) - S_2(Y_1Z_3 - Y_3Z_1) + U_2(Y_1Z_2 - Y_2Z_1)] \\ & + [R_3(Y_2Z_3 - Y_3Z_2) - S_3(Y_1Z_3 - Y_3Z_1) + U_3(Y_1Z_2 - Y_2Z_1)]\} \\ & \div [X_1(Y_2Z_3 - Y_3Z_2) - X_2(Y_1Z_3 - Y_3Z_1) + X_3(Y_1Z_2 - Y_2Z_1)] \end{aligned}$$

$$\begin{aligned} T_{03} = \{ & t_{04}[X_1(S_1Z_3 - U_1Z_2) + X_2(U_1Z_1 - R_1Z_3) + X_3(R_1Z_2 - S_1Z_1)] \\ & + t_{01}[X_1(S_2Z_3 - U_2Z_2) + X_2(U_2Z_1 - R_2Z_3) + X_3(R_2Z_2 - S_2Z_1)] \\ & + [X_1(S_3Z_3 - U_3Z_2) + X_2(U_3Z_1 - R_3Z_3) + X_3(R_3Z_2 - S_3Z_1)]\} \\ & \div [X_1(Y_2Z_3 - Y_3Z_2) - X_2(Y_1Z_3 - Y_3Z_1) + X_3(Y_1Z_2 - Y_2Z_1)] \end{aligned}$$

$$\begin{aligned} T_{02} = \{ & t_{04}[X_1(U_1Y_2 - S_1Y_3) + X_2(R_1Y_3 - U_1Y_1) + X_3(S_1Y_1 - R_1Y_2)] \\ & + t_{01}[X_1(U_2Y_2 - S_2Y_3) + X_2(R_2Y_3 - U_2Y_1) + X_3(S_2Y_1 - R_2Y_2)] \\ & + [X_1(U_3Y_2 - S_3Y_3) + X_2(R_3Y_3 - U_3Y_1) + X_3(S_3Y_1 - R_3Y_2)]\} \\ & \div [X_1(Y_2Z_3 - Y_3Z_2) - X_2(Y_1Z_3 - Y_3Z_1) + X_3(Y_1Z_2 - Y_2Z_1)] \end{aligned}$$

where:

$$R_1 = e_1 - d_1 + N_V(a_1 - e_1) \qquad X_1 = d_6 - e_5 + N_V(e_5 - a_6)$$

$$R_2 = -d_2 + N_V a_2 \qquad X_2 = C_6 - e_5 + N_H(e_5 - a_6)$$

$$R_3 = -d_5 + e_4 + N_V(-e_4 + a_5) \qquad X_3 = b_6 - e_5 + N_S(e_5 - a_6)$$

$$S_1 = e_1 - e_1 + N_H(a_1 - e_1) \qquad Y_1 = d_3 - e_2 + N_V(e_2 - a_3)$$

$$S_2 = -e_2 + N_H a_2 \qquad Y_2 = e_3 - e_2 + N_H(e_2 - a_3)$$

$$S_3 = -e_5 + e_4 + N_H(-e_4 + a_5) \qquad Y_3 = b_3 - e_2 + N_S(e_2 - a_3)$$

$$U_1 = e_1 - b_1 + N_S(a_1 - e_1) \qquad Z_1 = d_4 - e_3 + N_V(e_3 - a_4)$$

$$U_2 = -b_2 + N_S a_2 \qquad Z_2 = e_4 - e_3 + N_H(e_3 - a_4)$$

$$U_3 = -b_5 + e_4 + N_S(-e_4 + a_5) \qquad Z_3 = b_4 - e_3 + N_S(e_3 - a_4)$$

$$a_1 = \alpha_{60} A_{44}$$

$$a_2 = B_{12} + \epsilon_4$$

$$a_3 = (1 - \rho_1)\alpha_{23}\alpha_{53} B_3 + \rho_2 \alpha_{22}\alpha_{52} B_2$$

$$a_4 = \rho_1 \alpha_{23}\alpha_{53} B_3 + (1 - \rho_2)\alpha_{22}\alpha_{52} B_2$$

$$a_5 = E_{60} t_{60} A_{44} + B_{51}(E_{25} t_{25}\alpha_{55} + E_{55} t_{55}) + B_3(E_{23} t_{23}\alpha_{53} + E_{53} t_{53}) + B_2(E_{22} t_{22}\alpha_{52} + E_{52} t_{52})$$

$$a_6 = \alpha_{25}\alpha_{55} B_{51}$$

$$b_1 = \alpha_{60} B_{45}$$

$$b_2 = B_1 + \epsilon_5$$

$$b_3 = (1 - \rho_1)\alpha_{23}\alpha_{53} B_3 + \rho_2 \alpha_{22}\alpha_{52} B_2 = a_3$$

$$b_4 = \rho_1 \alpha_{23}\alpha_{53} B_3 + (1 - \rho_2)\alpha_{22}\alpha_{52} B_2 = a_4$$

$$b_5 = E_{60} t_{60} B_{45} + A_{55}(E_{25} t_{25}\alpha_{55} + E_{55} t_{55}) + B_3(E_{23} t_{23}\alpha_{53} + E_{53} t_{53}) + B_2(E_{22} t_{22}\alpha_{52} + E_{52} t_{52})$$

$$b_6 = \alpha_{25}\alpha_{55} A_{55}$$

$$c_1 = \alpha_{60} B_{43}$$

$$c_2 = B_1 + \epsilon_3$$

$$c_3 = (1 - \rho_1)\alpha_{23}\alpha_{53} A_{33} + \rho_2 \alpha_{22}\alpha_{52} B_2$$

$$c_4 = \rho_1 \alpha_{23}\alpha_{53} A_{33} + (1 - \rho_2)\alpha_{22}\alpha_{52} B_2$$

$$c_5 = E_{60} t_{60} B_{43} + B_{53}(E_{25} t_{25}\alpha_{55} + E_{55} t_{55}) + A_{33}(E_{23} t_{23}\alpha_{53} + E_{53} t_{53}) + B_2(E_{22} t_{22}\alpha_{52} + E_{52} t_{52})$$

$$c_6 = \alpha_{25}\alpha_{55} B_{53}$$

$$d_1 = \alpha_{60} B_{42}$$

$$d_2 = B_1 + \epsilon_2$$

$$d_3 = (1 - \rho_1)\alpha_{23}\alpha_{53} B_{32} + \rho_2 \alpha_{22}\alpha_{52} A_{22}$$

$$d_4 = \rho_1 \alpha_{23}\alpha_{53} B_{32} + (1-\rho_2)\alpha_{22}\alpha_{52} A_{22}$$

$$d_5 = E_{60} t_{60} B_{42} + B_{52}(E_{25} t_{25}\alpha_{55} + E_{55} t_{55}) + B_{32}(E_{23} t_{23}\alpha_{53} + E_{53} t_{53}) + A_{22}(E_{22} t_{22}\alpha_{52} + E_{52} t_{52})$$

$$d_6 = \alpha_{25}\alpha_{55} B_{52}$$

$$e_1 = \alpha_{60} B_{41} \ , \ e_2 = B_{21} + e_1$$

$$e_3 = (1-\rho_1)\alpha_{23}\alpha_{53} B_{31} + \rho_2 \alpha_{22}\alpha_{52} B_{21}$$

$$e_4 = \rho_1 \alpha_{23}\alpha_{53} B_{31} + (1-\rho_2)\alpha_{22}\alpha_{52} B_{21}$$

$$e_5 = E_{60} t_{60} B_{41} + B_{51}(E_{25} t_{25}\alpha_{55} + E_{55} t_{55}) + B_{31}(E_{23} t_{23}\alpha_{53} + E_{53} t_{53}) + B_{21}(E_{22} t_{22}\alpha_{52} + E_{52} t_{52})$$

$$e_6 = \alpha_{25}\alpha_{55} B_{51}$$

5.3 Radiometer Equations–SMMR Simulator–General Form

This section presents the general form of the radiometer equation realized when the questions in Section 5.2 are fully expanded. This expansion is undertaken in Reference 42.

6.6/10.7/18/21 GHz Radiometers

$$T = At_w + Bt_w N_H + Ct_w N_V + Dt_L + Et_L N_H + Ft_L N_V + N_H \Sigma G_i E_i t_i + N_V \Sigma H_i E_i t_i + \Sigma I_i E_i t_i$$

21 GHz Uplook

$$T = At_w + Bt_w N + Ct_L + Dt_L N + N\Sigma E_i E_i t_i + \Sigma F_i E_i t_i$$

37 GHz Radiometer

$$T = At_w + Bt_w N_H + Ct_w N_V + Dt_w N_S + Et_L + Ft_L N_H + Gt_2 N_V + Ht_2 N_S + N_H \Sigma I_i E_i t_i + N_V \Sigma J_i E_i t_i + N_S \Sigma K_i E_i t_i + \Sigma L_i E_i t_i$$

6.0 REFERENCES

1. D. H. Staelin, "Passive Remote Sensing at Microwave Wavelengths," Proc. IEEE, 57, 427–439, (1969).

2. K. Tomiyasu, "Remote Sensing of the Earth by Microwaves," Proc. IEEE, 62, 88–92, (1974).

3. T. Wilheit, W. Nordberg, J. Blinn, W. Campbell, A. Edgerton, "Aircraft Measurement of Microwave Emissions from Arctic Sea Ice," Remote Sensing of Environment, 129–139 (1972).

4. P. Gloersen, W. Nordberg, T. J. Schmugge, and T. Wilheit, "Microwave Signatures of First-Year and Multiyear Sea Ice," J. Geophys. Res., 78, 3564–3572 (1973).

5. W. J. Campbell, P. Gloersen, W. Nordberg, and T. T. Wilheit, "Dynamics and Morphology of Beaufort Sea Ice Determined from Satellites, Aircraft, and Drifting Stations," pp. 311–327, Cospar Approaches to Earth Survey Problems through Use of Space Techniques, Editor P. Bock, (Akademie-Verlag-Berlin, 1974).

6. T. Schmugge, P. Gloersen, T. Wilheit, and F. Geiger, "Remote Sensing of Soil Moisture with Microwave Radiometers," J. Geophys. Res., 79, 317–232, (1974).

7. T. J. Schmugge, T. T. Wilheit, P. Gloersen, M. F. Meyer, D. Frank, and I. Dirhirm, "Microwave Signatures of Snow and Fresh Water Ice," Proc. of the Sym. on Advanced Concepts and Techniques on the Study of Snow and Ice Resources, pp. 551–562, N.A.S., 1974, editor Henry S. Santeford.

8. W. J. Campbell, P. Gloersen, W. J. Webster, and T. T. Wilheit, "Beaufort Sea Ice Zones as Delineated by Microwave Imagery," to be published in J. Geophys. Res. 1976.

9. P. Gloersen, "Passive Microwave Images of Lake Ice," NAS SP 331, pp. 187–189 (1972).

10. P. Gloersen, T. J. Schmugge, and T. C. Chang, "Microwave Signatures of Snow, Ice, and Soil at Several Wavelengths," pp. 101–111, Proc. of the URSI Commission II Specialists Meeting on

Microwave Scattering and Emission from the Earth, E. Schanda, Editor, Berne, Switzerland, 1974.

11. A. E. Basharinov, S. T. Yegorov, A. S. Gurich, and A. M. Oboukhov, "Some Results of Microwave Sounding of the Atmosphere and Ocean from the Satellite Cosmos 243," Space Research XI, 394–600 (1971).

12. A. E. Basharinov, A. S. Gurvitch, A. K. Gorodezky, S. T. Egorov, B. G. Kutuza, A. A. Kurskaya, D. T. Matveev, A. P. Orlov, and A. M. Shutko, "Satellite Measurements of Microwave and Infrared Radio Brightness Temperature of the Earth's Cover and Clouds," Proc. 8th Int. Symp. Rem. Sensing Environ., 291–296, U. Mich. (1972).

13. T. Wilheit, "The Electrically Scanning Microwave Radiometer (ESMR) Experiment," in: The Nimbus-5 User's Guide, pp. 59–105, NASA Goddard Space Flight Center, Greenbelt, MD (1972).

14. D. H. Staelin, A. H. Barrett, J. W. Waters, F. T. Barath, E. J. Johnston, P. W. Rosenkranz, N. E. Gaut, and W. B. Lenor, "Microwave Spectrometer on the Nimbus-5 Satellite: Meteorological and Geophysical Data," Science, 182, 1339–1341, (1973).

15. "Skylab Program: Earth Resources Experiment Package, Sensor Performance Report," Vol. 6 (S-19), MSC-05528, NASA Johnson Space Center, Houston (1974).

16. T. Wilheit, "The Electrically Scanning Microwave Radiometer (ESMR) Experiment," in the Nimbus-6 User's Guide, pp. 87–108, NASA/Goddard Space Flight Center, Greenbelt, MD (1975).

17. D. H. Staelin, A. H. Barrett, P. W. Rosenkranz, F. T. Barath, E. J. Johnston, J. W. Waters, and A. Wouters, "The Scanning Microwave Spectrometer (SCAMS) Experiment," in the Nimbus-6 User's Guide, pp. 59–86, NASA Goddard Space Flight Center, Greenbelt, MD (1975).

18. P. Gloersen, "Description of a Mechanically Scanned Microwave Radiometer for Use on Nimbus-G," NASA Goddard Space Flight Center (1973).

19. P. Gloersen, "Surface and Atmosphere Parameter Maps," NASA/Goddard Space Flight Center (1976).

20. J. W. Waters, et al., "The Shuttle Imaging Microwave System Experiment."

21. K. L. S. Gunn and T. U. R. East, "The Microwave Properties of Precipitation Particles," Quart. J. Met. Soc., 80, 552–545, 1954.

22. M. Meeks, II and A. E. Lilley, "The Microwave Spectrum of Oxygen in the Earth's Atmosphere," J. Geophys. Res. 68, 1963.

23. D. A. Staelin, "Measurements and Interpretation of the Microwave Spectrum of the Terrestrial Atmosphere Near 1 Centimeter Wavelength," J. Geophys. Res., 71, 2875–2881, 1966.

24. J. A. Lane and J. A. Saxton, "Dielectric Dispersion in Pure Polar Liquids at Very High Radio Frequencies," Proc. Roy. Soc. London A, 214, pp. 531–545, 1952.

25. International Critical Tables of Numerical Data, Physics, Chemistry and Technology, Vol. IV, McGraw Hill, NY 1928, pp. 231–239.

26. J. D. Jackson, "Classical Electrodynamics," John Wiley & Sons, Inc., New York, 1962, p. 216ff.

27. J. P. Hollinger, "Passive Microwave Measurements of Sea Surface Roughness," Trans. IEEE Geoscience Electronics, GE-9, pp. 165–169 (1971).

28. W. Nordberg, J. Conaway, D. B. Ross, and T. Wilheit, "Measurements of Microwave Emission from a Foam-Covered Wind Driven Sea," J. Atmos. Sci., 28, 429–435, 1971.

29. T. Schmugge, P. Gloersen, and T. Wilheit, "Remote Sensing of Soil Moisture with Microwaves," NAS X-652-72-305.

30. A. T. Edgerton, F. Ruskey, D. Williams, A. Stogryn, G. Poe, D. Meeks, and O. Russell, "Microwave Emission Characteristics of Natural Materials and the Environment," Microwave Division, Aerojet General Corpor., ONR Contract NOOD 14-70C-0315, 1971.

31. T. Wilheit, W. Nordberg, J. Blinn, W. Campbell, and A. Edgerton, "Aircraft Measurements of Microwave Emission from Arctic Sea Ice," to be published in Remote Sensing of Environment.

32. C. Calhoon, "Performance and Operational Requirements for a X-Band Radiometer System," NASA/Goddard Space Flight Center, 1974.

33. C. Calhoon, "Performance and Operations Requirements for a K-Band Radiometer System," NASA/Goddard Space Flight Center, 1974.

34. J. Kirwan, "Operations and Service Manual, SS Part No. 311-X-1-001, X-Band Microwave Radiometer," Sense Systems Company, NASA Contract NAS 5-19929, 1976.

35. J. Kirwan, "Operations and Service Manual, SS Part No. 311-K-1-001, K-Band Microwave Radiometer," Sense Systems Company, NASA Contract NAS 5-19929, 1976.

36. C. D. Calhoon, Jr., "SMMR Simulator: A Multifrequency Microwave Radiometer System," National Aeronautics and Space Administration, Goddard Space Flight Center, X-953-76-283, 1976.

37. C. D. Calhoon, Jr. and B. M. Krupp, "SMMR Simulator Systems Calibration: Requirements and Procedures," _____, TM-79609, 1978.

38. B. M. Krupp and C. D. Calhoon, "Scanning Multi-channel Microwave Radiometer (SMMR) Simulator System Calibrations I: Derivation and Comparison of Calibration Formulations," Computer Sciences Corporation, CSC/TM-78/6213, 1978.

39. J. D. Kraus, Radio Astronomy, New York: McGraw Hill, 1964.

40. S. Chandrasekhar, Radiative Transfer, New York: Dover 1960.

41. B. M. Krupp and R. A. Neiman, "The Use of the Rayleigh-Jeans Approximation at Millimeter Wavelength," Computer Sciences Corporation, CSC/TM-78/6021, 1978.

42. C. D. Calhoon, M. Doyle, and S. Link, "SMMR Simulator Radiometer Equation Derivations," NASA/Goddard Space Flight Center, X-946-79-8, 1979.

43. S. Link, "Radiative Transfer Theory Applied to a Cascade of Ferrite Switch Junctions," Memorandum to the Record, 1979.

44. S. Link, "Background Information for SMMR Simulator Calibration Model Development—Radiative Transfer in a Lossy Element," Memorandum to the Record, 1979.

APPENDIX 1

EFFECTS OF COMPONENT MISMATCH ON THE OPERATION CHARACTERISTICS OF A RADIOMETER SYSTEM

All equations and derivations in the main body of this document assume a negligible component mismatch (VSWR $\approx$ 1). This appendix will investigate the effect of component mismatch on the operation characteristics discussed in the document main body.

It is noted at the outset that any numerical analysis attempted will provide an inexact solution in-as-much-as only the magnitude of the mismatch effect (VSWR) can be calculated. Any phase relationships causing variation in the radiometer system operation characteristics must be determined empirically.

A typical SMMR simulator radiometer system is schematically represented in Figure 1. That component which contributes an appreciable mismatch into the radiometer system is the antenna. Transmission line theory shows that the antenna VSWR, as determined at the antenna output, will be reduced when measured at the output of the waveguide section connecting the antenna to the ferrite switch assembly.

Define S_A = Antenna VSWR at the antenna output

S_G = VSWR of the antenna at the waveguide output

L = insertion loss in dB through the waveguide

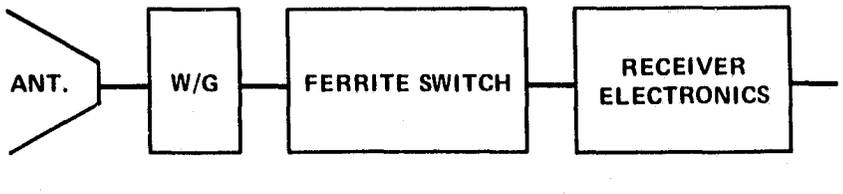

Figure 1

The following relationship can be expressed for the effective VSWR:

$$\text{COTH}^{-1} S_G = \text{COTH}^{-1} S_A + L/8.686 \quad (1)$$

The VSWR of the antenna/waveguide component will cause a change in the operation characteristics (VSWR, isolation, insertion loss) of the ferrite switch assembly. Define the following additional terms:

S_F = ferrite switch input VSWR

S_{FE} = effective ferrite switch VSWR

L_A = insertion loss of antenna/waveguide

L_F = insertion loss of ferrite switch

L_S = system insertion loss

The following relations hold:

$$S_{FE} = \frac{S_F^2 S_G + S_F}{S_F + S_G} \quad (2)$$

and

$$L_S = L_A + L_F + 20 \log_{10}(1 \pm |\Gamma_G \Gamma_{FE}|) \quad (3)$$

where

$$|\Gamma_G| = \frac{S_G - 1}{S_G + 1} \quad \text{and} \quad |\Gamma_{FE}| = \frac{S_{FE} - 1}{S_{FE} + 1} \quad (4)$$

Define L_{FE} as an effective ferrite switch insertion loss where

$$L_{FE} = L_F + 20 \log_{10} (1 \pm |\Gamma_G \Gamma_{FE}|) \quad (5)$$

The effective ferrite switch isolation may be determined from Table 1 using the value S_{FE} calculated in Equation (2).

The ferrite switch junction in the SMMR Simulator radiometer systems is a three port circulator (Figure 2). When the ferrite is biased for clockwise circulation, any input signal at port 1

Table 1

Ferrite Junction VSWR-Isolation

VSWR	ISOL.	VSWR	ISOL.	VSWR	ISOL.	VSWR	ISOL.
1.001	66.025	1.051	32.088	1.102	26.281	1.210	20.443
1.002	60.009	1.052	31.923	1.104	26.120	1.220	20.079
1.003	56.491	1.053	31.762	1.106	25.963	1.230	19.732
1.004	53.997	1.054	31.604	1.108	25.809	1.240	19.401
1.005	52.063	1.055	31.449	1.110	25.658	1.250	19.085
1.006	50.484	1.056	31.297	1.112	25.510	1.260	18.783
1.007	49.149	1.057	31.147	1.114	25.364	1.270	18.493
1.008	47.993	1.058	31.000	1.116	25.221	1.280	18.216
1.009	46.975	1.059	30.865	1.118	25.081	1.290	17.949
1.010	46.064	1.060	30.714	1.120	24.943	1.300	17.692
1.011	45.240	1.061	30.575	1.122	24.808	1.310	17.445
1.012	44.489	1.062	30.438	1.124	24.675	1.320	17.207
1.013	43.798	1.063	30.303	1.126	24.544	1.330	16.977
1.014	43.159	1.064	30.171	1.128	24.415	1.340	16.755
1.015	42.564	1.065	30.040	1.130	24.289	1.350	16.540
1.016	42.007	1.066	29.912	1.132	24.164	1.360	16.332
1.017	41.485	1.067	29.785	1.134	24.042	1.370	16.131
1.018	40.993	1.068	29.661	1.136	23.921	1.380	15.936
1.019	40.528	1.069	29.538	1.138	23.803	1.390	15.747
1.020	40.086	1.070	29.417	1.140	23.686	1.400	15.563
1.021	39.667	1.071	29.298	1.142	23.571	1.410	15.385
1.022	39.267	1.072	29.181	1.144	23.457	1.420	15.211
1.023	38.885	1.073	29.066	1.146	23.346	1.430	15.043
1.024	38.520	1.074	28.952	1.148	23.235	1.440	14.879
1.025	38.170	1.075	28.839	1.150	23.127	1.450	14.719
1.026	37.833	1.076	28.728	1.152	23.020	1.460	14.564
1.027	37.510	1.077	28.619	1.154	22.914	1.470	14.412
1.028	37.198	1.078	28.511	1.156	22.810	1.480	14.264
1.029	36.898	1.079	28.405	1.158	22.708	1.490	14.120
1.030	36.607	1.080	28.299	1.160	22.607	1.500	13.979
1.031	36.327	1.081	28.196	1.162	22.507	1.520	13.708
1.032	36.055	1.082	28.093	1.164	22.408	1.540	13.449
1.033	35.792	1.083	27.992	1.166	22.311	1.560	13.201
1.034	35.537	1.084	27.892	1.168	22.215	1.580	12.964
1,035	35.290	1.085	27.794	1.170	22.120	1.600	12.736
1.036	35.049	1.086	27.696	1.172	22.027		
1.037	34.816	1.087	27.600	1.174	21.934	1.620	12.518
1.038	34.588	1.088	27.505	1.176	21.843	1.640	12.308
1.039	34.367	1.089	27.411	1.178	21.753	1.660	12.107
1.040	34.151	1.090	27.318	1.180	21.664	1.680	11.913
						1.700	11.725
1.041	33.941	1.091	27.226	1.182	21.576		
1.042	33.736	1.092	27.135	1.184	21.489	1.720	11.545
1.043	33.536	1.093	27.046	1.186	21.403	1.740	11.370
1.044	33.341	1.094	26.957	1.188	21.318	1.760	11.202
1.045	33.150	1.095	26.869	1.190	21.234	1.780	11.039
1.046	32.963	1.096	26.782	1.192	21.151	1.800	10.881
1.047	32.780	1.097	26.697	1.194	21.069		
1.048	32.602	1.098	26.612	1.196	20.988	1.820	10.729
1.049	32.427	1.099	26.528	1.198	20.907	1.840	10.581
1.050	32.256	1.100	26.444	1.200	20.828	1.860	10.437
						1.880	10.298
						1.900	10.163

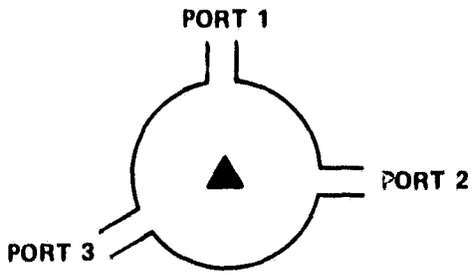

Figure 2

travels to port 2, signal at port 2 travels to port 3, and signal at port 3 travels to port 1. The ferrite's magnetic field does not entirely cut off counterclockwise signal travel. Therefore, a portion of the input signal at port 2 reaches port 1, at port 1 reaches port 3, and at port 3 reaches port 2. The direct (clockwise) path transmissivity is defined as α while the indirect (counterclockwise) path isolation transmissivity is defined as β. Therefore, the outputs at each port will be

$$OUT_1 = IN_3\alpha + IN_2\beta \tag{6a}$$

$$OUT_2 = IN_1\alpha + IN_3\beta \tag{6b}$$

$$OUT_3 = IN_2\alpha + IN_1\beta \tag{6c}$$

A similar equation set may be developed when the ferrite is biased to provide counterclockwise direct path circulation.

Equation set (6) will hold true as long as there is no component mismatch at the input ports. Should such a mismatch occur, additional terms will be required in the equation set. These terms will account for any reflected signal caused by the mismatch. The coefficient of reflectivity, Γ (Equation (4), for a given mismatch (VSWR) is defined as that fractional amount of a signal which is reflected when a mismatch is encountered (see Table 2).

Given a mismatch at port 1 (Figure 2), a portion of the signal output at port 1 (Equation (6a)) will be reflected as a secondary input:

$$IN_1' = \Gamma\,(OUT\ 1) = \Gamma\,(IN_3\alpha + IN_2\beta) \tag{7}$$

Table 2

VSWR–Coefficient of Reflectivity

VSWR	Rho V	Rho P	VSWR	Rho V	Rho P	VSWR	Rho V	Rho P	VSWR	Rho V	Rho P
1.001	0.0005	0.00000	1.051	0.0249	0.00062	1.102	0.0485	0.00235	0.210	0.0950	0.00903
1.002	0.0010	0.00000	1.052	0.0253	0.00064	1.104	0.0494	0.00244	0.220	0.0991	0.00982
1.003	0.0015	0.00000	1.053	0.0258	0.00067	1.106	0.0503	0.00253	1.230	0.1031	0.01064
1.004	0.0020	0.00000	1.054	0.0263	0.00069	1.108	0.0512	0.00262	1.240	0.1071	0.01148
1.005	0.0025	0.00001	1.055	0.0268	0.00072	1.110	0.0521	0.00272	1.250	0.1111	0.01235
1.006	0.0030	0.00001	1.056	0.0272	0.00074	1.112	0.0530	0.00281	1.260	0.1150	0.01324
1.007	0.0035	0.00001	1.057	0.0277	0.00077	1.114	0.0539	0.00291	1.270	0.1189	0.01415
1.008	0.0040	0.00002	1.058	0.0282	0.00079	1.116	0.0548	0.00301	1.280	0.1228	0.01508
1.009	0.0045	0.00002	1.059	0.0287	0.00082	1.118	0.0557	0.00310	1.290	0.1266	0.01604
1.010	0.0050	0.00002	1.060	0.0291	0.00085	1.120	0.0566	0.00320	1.300	0.1304	0.01701
1.011	0.0055	0.00003	1.061	0.0296	0.00088	1.122	0.0575	0.00331	1.310	0.1342	0.01801
1.012	0.0060	0.00004	1.062	0.0301	0.00090	1.124	0.0584	0.00341	1.320	0.1379	0.01902
1.013	0.0065	0.00004	1.063	0.0305	0.00093	1.126	0.0593	0.00351	1.330	0.1416	0.02006
1.014	0.0070	0.00005	1.064	0.0310	0.00096	1.128	0.0602	0.00362	1.340	0.1453	0.02111
1.015	0.0074	0.00006	1.065	0.0315	0.00099	1.130	0.0610	0.00373	1.350	0.1489	0.02218
1.016	0.0079	0.00006	1.066	0.0319	0.00102	1.132	0.0619	0.00383	1.360	0.1525	0.02327
1.017	0.0084	0.00007	1.067	0.0324	0.00105	1.134	0.0628	0.00394	1.370	0.1561	0.02437
1.018	0.0089	0.00008	1.068	0.0329	0.00108	1.136	0.0637	0.00405	1.380	0.1597	0.02549
1.019	0.0094	0.00009	1.069	0.0333	0.00111	1.138	0.0645	0.00417	1.390	0.1632	0.02663
1.020	0.0099	0.00010	1.070	0.0338	0.00114	1.140	0.0654	0.00428	1.400	0.1667	0.02778
1.021	0.0104	0.00011	1.071	0.0343	0.00118	1.142	0.0663	0.00439	1.410	0.1701	0.02894
1.022	0.0109	0.00012	1.072	0.0347	0.00121	1.144	0.0672	0.00451	1.420	0.1736	0.03012
1.023	0.0114	0.00013	1.073	0.0352	0.00124	1.146	0.0680	0.00463	1.430	0.1770	0.03131
1.024	0.0119	0.00014	1.074	0.0357	0.00127	1.148	0.0689	0.00475	1.440	0.1803	0.03252
1.025	0.0123	0.00015	1.075	0.0361	0.00131	1.150	0.0698	0.00487	1.450	0.1837	0.03374
1.026	0.0128	0.00016	1.076	0.0366	0.00134	1.152	0.0706	0.00499	1.460	0.1870	0.03497
1.027	0.0133	0.00018	1.077	0.0371	0.00137	1.154	0.0715	0.00511	1.470	0.1903	0.03621
1.028	0.0138	0.00019	1.078	0.0375	0.00141	1.156	0.0724	0.00524	1.480	0.1935	0.03746
1.029	0.0143	0.00020	1.079	0.0380	0.00144	1.158	0.0732	0.00536	1.490	0.1968	0.03873
1.030	0.0148	0.00022	1.080	0.0385	0.00148	1.160	0.0741	0.00549	1.500	0.2000	0.04000
1.031	0.0153	0.00023	1.081	0.0389	0.00152	1.162	0.0749	0.00561	1.520	0.2063	0.04258
1.032	0.0157	0.00025	1.082	0.0394	0.00155	1.164	0.0758	0.00574	1.540	0.2126	0.04520
1.033	0.0162	0.00026	1.083	0.0398	0.00159	1.166	0.0766	0.00587	1.560	0.2188	0.04785
1.034	0.0167	0.00028	1.084	0.0403	0.00162	1.168	0.0775	0.00600	1.580	0.2248	0.05054
1.035	0.0172	0.00030	1.085	0.0408	0.00166	1.170	0.0783	0.00614	1.600	0.2308	0.05325
1.036	0.0177	0.00031	1.086	0.0412	0.00170	1.172	0.0792	0.00627			
1.037	0.0182	0.00033	1.087	0.0417	0.00174	1.174	0.0800	0.00641	1.620	0.2366	0.05600
1.038	0.0186	0.00035	1.088	0.0421	0.00178	1.176	0.0809	0.00654	1.640	0.2424	0.05877
1.039	0.0191	0.00037	1.089	0.0426	0.00182	1.178	0.0817	0.00668	1.660	0.2481	0.06156
1.040	0.0196	0.00038	1.090	0.0431	0.00185	1.180	0.0826	0.00682	1.680	0.2537	0.06438
									1.700	0.2593	0.06722
1.041	0.0201	0.00040	1.091	0.0435	0.00189	1.182	0.0834	0.00696			
1.042	0.0206	0.00042	1.092	0.0440	0.00193	1.184	0.0842	0.00710	1.720	0.2647	0.07007
1.043	0.0210	0.00044	1.093	0.0444	0.00197	1.186	0.0851	0.00724	1.740	0.2701	0.07294
1.044	0.0215	0.00046	1.094	0.0449	0.00202	1.188	0.0859	0.00738	1.760	0.2754	0.07582
1.045	0.0220	0.00048	1.095	0.0453	0.00206	1.190	0.0868	0.00753	1.780	0.2806	0.07872
1.046	0.0225	0.00051	1.096	0.0458	0.00210	1.192	0.0876	0.00767	1.800	0.2857	0.08163
1.047	0.0230	0.00053	1.097	0.0463	0.00214	1.194	0.0884	0.00782			
1.048	0.0234	0.00055	1.098	0.0467	0.00218	1.196	0.0893	0.00797	1.820	0.2908	0.08455
1.049	0.0239	0.00057	1.099	0.0472	0.00222	1.198	0.0901	0.00811	1.840	0.2958	0.08748
1.050	0.0244	0.00059	1.100	0.0476	0.00227	1.200	0.0909	0.00826	1.860	0.3007	0.09042
									1.880	0.3056	0.09336
									1.900	0.3103	0.09631

VSWR Voltage Standing Wave Ratio
Rho V (ρ_v) Voltage Reflection Coefficient
Rho P (ρ_p) Power Reflection Coefficient = ρ_v^2

Thus the input signal at port 1 becomes: IN_1''

where
$$IN_1'' = IN_1 + IN_1' \tag{8}$$

Therefore, from Equation (6):

$$OUT_2 = IN_1''\alpha + IN_3\beta = [IN_1 + \Gamma(IN_3\alpha + IN_2\beta)]\,\alpha + IN_3\beta \tag{9a}$$

$$OUT_3 = IN_2\alpha + IN_1''\beta = IN_2\alpha + [IN_1 + \Gamma(IN_3\alpha + IN_2\beta)]\,\beta \tag{9b}$$

Similar equations may be generated with mismatches at other ports. These further mismatches will cause a "domino effect" through the entire equation set.

The following effects when a mismatch occurs in a radiometer system typical of the SMMR simulator have been noted:

a. The ferrite junction isolation will be reduced from that physically measured.

b. The ferrite junction insertion loss will vary, may increase or decrease, dependent upon VSWR phase relations.

c. Input signal mixing will occur due to circulator operation and mismatch reflection.

It is concluded that to determine the true nature of these effects on the radiometer system calibration, a "full-up" mission configuration testing program must be undertaken so as to determine the phase dependent relationships noted in the previous discussion.